12-2010

HIGH FREQUENCY FERROMAGNETIC INDUCTIVE ELEMENTS FOR ON-CHIP INTEGRATION AND THEIR MAGNETIZATION DYNAMICS

Hanqiao Zhang
Clemson University, hanqiaz@clemson.edu

HIGH FREQUENCY FERROMAGNETIC INDUCTIVE ELEMENTS FOR ON-CHIP INTEGRATION AND THEIR MAGNETIZATION DYNAMICS

A Dissertation
Presented to
the Graduate School of
Clemson University

In Partial Fulfillment
of the Requirements for the Degree
Doctor of Philosophy
Electrical Engineering

---

by
Hanqiao Zhang
November 2010

Accepted by:
Dr. Pingshan Wang, Committee Chair
Dr. L. Wilson Pearson
Dr. Todd H. Hubing
Dr. Apparao M. Rao

ABSTRACT

The dissertation focuses on the broadband characterization of magnetization dynamics of submicron (200-550 nm wide, 10 μm long, 100 nm thick) and micron (2-10 μm wide, 100 μm long, 100 nm thick) size patterned ferromagnetic material (Permalloy, Py) with low frequency and microwave measurement methods. Particularly the ferromagnetic resonance (FMR), damping process, magnetization reversal, mag-noise, and 1/*f* noise in different pattern geometry, DC current and external magnetic field bias situations are investigated. In addition to simple microwave transmission line measurements, a sensitive on-chip microwave interferometer is proposed and fabricated by means of nano-fabrication techniques. The FMR properties of an individual nanoscale Py pattern were measure with the interferometer.

DEDICATION

To:

My parents, Jinbo and Yahua

ACKNOWLEDGEMENTS

First of all, I would especially like to acknowledge my advisor, Professor Pingshan Wang, for his excellent advice and mentoring throughout my Ph.D. time at Clemson University. I have greatly enjoyed his good humor and friendship, and I am very grateful to have had the opportunity to work with someone with such extensive knowledge in microwave engineering and nanoscale science and such great enthusiasm for scientific research. His incisive comments and inspirational ideas always bring a fresh perspective to my research projects. I could not have accomplished all the requirements of a Ph.D. degree without his encouragement and guidance. I would like to gratefully acknowledge Professor L. Wilson Pearson for his helping hands and valuable equipments on my measurements. I would like to gratefully acknowledge Professor Todd H Hubing and Professor Apparao M Rao for their valuable comments on the work presented in this dissertation. I appreciate my committee professors for their kindness to take time out of their busy schedules to read this dissertation and serve on my defense committee.

I would also like to acknowledge my present group members for their help and friendship during the past few years: Mr. Chaojiang Li, Ms. Chunrong Song, Mr. Yang Yang, Mr. Yongtao Geng and Ms. Huan Zou. Special thanks must go to Chaojiang and Chunrong for all the encouragement and help from the very beginning of my study in Clemson in both research and life aspects. Besides all the inspiring discussions I had with them about research and life that I might not be able to enjoy as often after graduation, I am always proud of working in such a harmonious group.

During the progress of the nanoscale Permalloy thin film characterization work presented in this dissertation, I was very fortunate to be able to collaborate with Dr. Ralu Divan and Dr. Axel Hoffmann of Argonne National Laboratory. I am very grateful to them for their help, guiding hand and paper manuscript discussions, and I have learned a lot of experimental techniques from them during our nanofabrication periods at the Center for Nanoscale Materials (CNM) of Argonne National Laboratory. I would also like to thank Mr. Vince Genova, Mr. Garry J. Bondonaro and Mr. Michael Skvarla at Cornell Nanoscale Science and Technology Facility (CNF) for their nanofabrication training and support. Without them, all of the on-chip microwave interferometer work presented in this dissertation would not have been possible.

Finally I would like to thank my parents, for their infinite love and support.

TABLE OF CONTENTS

Page

Table of Contents (Continued)

Page

LIST OF FIGURES

List of Figures (Continued)

Figure Page

List of Figures (Continued)

Figure Page

CHAPTER ONE

INTRODUCTION

Nanoscale magnetic materials are now an extremely active area of research interest as evidenced by recent advances in the development of high-performance magnetic microwave devices [1.1-1.3], solid state memory and logic devices [1.4-1.5], spin manipulation [1.6] and signal processing devices [1.7]. The discovery of giant magnetoresistance (GMR) phenomenon in the late 1980's by Baibich et al. [1.8], was a stimulus for the field, in part because of its rapid incorporation into commercial devices, from magnetic sensors for magnetic hard drives to the novel non-volatile magnetic random access memory (MRAM). Nanoscale magnetic material based spintronics has emerged as a new multidisciplinary field which exploits the quantum spin states of electrons as well as their charge states [1.9]. It is among the most exciting areas at the frontier of nanoscience — they not only have fundamentally intriguing phenomena, but also are leading to a variety of promising technological applications.

The performance of spintronic devices and magnetic microwave devices will be eventually limited by several magnetization dynamics of the magnetic layers: ferromagnetic resonance (FMR), magnetization switching and noise. For example, with the development of magnetic information storage and MRAM technologies, especially when data rates approach the GHz-regime where faster read and write speeds are required to keep data access time reasonable, the broadband mag-noise should be carefully considered. On the other hand, there is a critical need for the extension of current magnetic microwave device physics and technology into the high-frequency range of 10-

100 GHz where FMR precession of ferromagnetic thin films is technologically important. Hence, new insight into the magnetization dynamics is highly demanded as precessional relaxation phenomena will begin to dominate the dynamic process during the operation of the devices based on these conductive elements. Therefore, fundamental research on the broadband magnetization dynamics has become a major area of growing interest in both scientific and technological aspects.

Ferromagnetic resonance (FMR) is the main technique for the investigation of magnetization dynamics of low dimensional patterned magnetic structures. The conventional approaches to the measurement of the FMR response are through shorted waveguides, microwave cavity, or stripline techniques [1.10]. FMR spectroscopy has also been proposed for study of energy assisted magnetic storage technologies recently. Various new FMR methods have also been developed, such as FMR force microscopy which uses a scannable probe field for FMR modes imaging, and scanning thermal FMR microscopy which has a spatial resolution in 10 nm range [1.10-1.11]. Other characterization techniques have also been developed in the last few decades for investigating the magnetic properties of thin-film materials. The magnetic force microscope (MFM) and the spin-polarized scanning tunneling microscope (SP-STM) have been invented to measure local magnetic forces and interactions down to the atomic scale. The time-resolved x-ray magnetic circular dichroism (TR-XMCD) technique is developed for element- and layer-resolved studies of magnetization dynamics. The application of ultrafast laser pulses was another major breakthrough in time-resolved studies of magnetization dynamics. Using the magneto-optical Kerr effect (MOKE), the

laser-induced magnetization relaxation dynamics can be directly investigated by the all-optical pump-probe technique.

In this dissertation, a number of different topics in magnetization dynamics have been covered by a systematic approach to the goal of studying the ferromagnetic elements for on-chip integration. Novel FMR spectroscopy with ultra high sensitivity is also proposed. Below is an outline of the document, each chapter covers an experiment topic:

Ferromagnetic thin films have been explored for high-performance magnetic microwave devices, such as inductors. The promising results have shown that the areal inductance could be improved by ~28 times with ferromagnetic materials, however, the FMR frequency of the studied unpatterned ferromagnetic films falls into the sub-GHz range. One strategy to improve their high-frequency performance is to increase the shape anisotropy field of the ferromagnetic materials. The properly patterned ferromagnetic thin films have 'built-in' high shape anisotropy fields and, therefore, can provide a self-biasing for high-frequency applications in the 10-100 GHz range. In Chapter 2 we demonstrate that a 10 GHz natural FMR frequency can be achieved by patterning Permalloy (Py=$Ni_{80}Fe_{20}$) thin film into nanoscale stripes of large aspect ratios. We present the methodology of using FMR spectroscopy for magnetization dynamics studies in the patterned magnetic thin films. FMR and complex susceptibility of these thin films are observed and extracted from the measured scattering parameters. Effects of sample geometry on the FMR and complex susceptibility are investigated. The sample fabrication processes and measurement procedures are discussed.

Current magnetic storage and complementary metal-oxide-semiconductor (CMOS) integrated circuit (IC) systems usually require direct current (DC) passing through the magnetoelectronic sensors and magnetic microwave devices. The DC current effects on magnetization dynamics of magnetic thin films in these systems are of critical importance from the system reliability point of view. Chapter 3 presents the DC current effects on the FMR and complex susceptibility of the magnetic samples studied in Chapter 2. Comparison between the effects of DC and external static magnetic field on the magnetic thin films is conducted. Unexpected magnetization dynamics differences between the two situations are observed. It is shown that to get the same FMR frequency shift, the required Oersted field is about 20% of the static magnetic field. We attribute the phenomena to the unique Joule heating effects of the DC current. Detailed magnetization dynamics regarding the observed FMR frequency shift were analyzed by theoretical methods and micromagnetic simulations.

The operation performance of all magnetic storage devices and novel spintronic devices will be eventually limited by the magnetization reversal characteristics of magnetic thin films. As the areal density of magnetic hard drives keeps increasing, different magnetic storage techniques are proposed to solve the trilemma of signal-noise ratio, writability and thermal stability. Energy assisted magnetization reversal is one of the promising method for future development. FMR spectroscopy is one powerful way of the energy assisted magnetization reversal study. In Chapter 4 we present the DC current energy effects on the magnetization reversal properties of the nanoscale patterned Py thin films. The temperature dependence of the sample coercivity is determined from the

Arrhenius model. We observed a 33% coercivity reduction for different nanoscale Py patterns at 50 mA biasing DC current. The magnetization reversal mechanisms are also analyzed according to the temperature dependence of coercivity.

As the magnetic pattern dimension keeps decreasing and demanded magnetoelectronic sensor sensitivity increasing, noise of magnetic thin films has become another critical issue. In Chapter 5 we study the broadband thermal magnetic-noise (mag-noise) of the nanoscale magnetic thin films by the Y-factor method. Close correlations between the mag-noise and FMR absorption was observed. An *RLCG* model is proposed to theoretically model the underlying magnetization dynamics. In Chapter 6 Low frequency noise in different micrometer scale Py patterns were measured by a four point scheme. Pattern geometry and bias current effects on the material's $1/f$ noise were studied. The normalized Hooge parameter and frequency slope were analyzed in the framework of the empirical Hooge relation.

The last chapter presents our development of an on-chip microwave interferometer, which has a significantly improved sensitivity compared with conventional transmission line methods. The device sensitivity is improved by canceling the inherent common-mode background signal in a splitting-rejoining-subtraction fashion. A micrometer size Py array was measured by the prototype device fabricated with standard photolithography and metallization methods. The effective linewidth and complex susceptibility of the sample under test are extracted from the measurement data. A development of the device, which has a simplified structure and tapered measurement section is also proposed. The new device has a more than 20 dB sensitivity improvement

over its prototype. The FMR and damping properties of a single nanoscale Py nanowire (70 nm thick, 0.24×5 μm^2 lateral size) at radio-frequencies are studied with the interferometer.

References

[1.1] D. S. Gardner, G. Schrom, P. Hazucha, F. Paillet, T. Karnik, S. Borkar, R. Hallstein, T. Dambrauskas, C. Hill, C. Linde, W. Worwag, R Baresel, and S. Muthukumar, "Detection of the Weak Magnetic Properties Change of Stainless-Steel Welding Parts by Low Frequency Magnetic Imaging," *J. Appl. Phys.* **103**, 07E923 (2008).

[1.2] P. Wang, H. Zhang, R. Divan and A. Hoffmann, "Tailoring High-Frequency Properties of Permalloy Films by Submicrometer Patterning," *IEEE Trans. Magn.* **45**, 71 (2009).

[1.3] H. Zhang, A. Hoffmann, R. Divan and P. Wang, "Direct Current Effects on High-Frequency Properties of Patterned Permalloy Thin Film," *IEEE Trans. Magn.* **45**, 5296 (2009).

[1.4] S. S. P. Parkin, M. Hayashi, and L. Thomas, "Magnetic Domain-Wall Racetrack Memory," *Science* **320**, 190 (2008).

[1.5] D. A. Allwood, G. Xiong, C. C. Faulkner, D. Atkinson, D. Petit, and R. P. Cowburn, "Magnetic Domain-Wall Logic," *Science.* **309**, 1688 (2005).

[1.6] E. S. Garlid, Q. O. Hu, M. K. Chan, C. J. Palmstrøm, and P. A. Crowell, "Electrical Measurement of the Direct Spin Hall Effect in Fe/$In_xGa_{1-x}As$ Heterostructures," *Phys. Rev. Lett.* **105**, 156602 (2010).

[1.7] S. I. Kiselev, J. C. Sankey, I. N. Krivorotov, N. C. Emley, R. J. Schoelkopf, R. A. Buhrman and D. C. Ralph, "Microwave Oscillations of a Nanomagnet Driven by A Spin-Polarized Current," *Nature.* **425**, 380 (2003).

[1.8] M. N. Baibich, J. M. Broto, A. Fert, F. N. V. Dau, F. Petro, P. Eitenne, G. Creuzet, A. Friederich, and J. Chazelas, "Giant Magnetoresistance of (001)Fe/(001)Cr Magnetic Superlattices," *Phys. Rev. Lett.* **61**, 2472 (1988).

[1.9] C. Chappert, A. Fert and F. N. V. Dau, "The Emergence of Spin Electronics in Data Storage," *Nature Materials.* **6**, 813 (2007).

[1.10] N. Mo and C. E. Patton, "Perspective: Local ferromagnetic resonance measurement techniques: "Invited Review Article: Microwave spectroscopy based on scanning thermal microscopy: Resolution in the nanometer range" [Rev. Sci. Instrum. 79, 041101 (2008)]," *Rev. Sci. Instrum.* **79**, 040901 (2008).

[1.11] I. Lee, Y. Obukhov, G. Xiang, A. Hauser, F Yang, P Banerjee, D. V. Pelekhov and P. C. Hammel, "Nanoscale Scanning Probe Ferromagnetic Resonance Imaging Using Localized Modes," *Nature.* **466**, 845 (2010).

CHAPTER TWO

TAILORING HIGH-FREQUENCY PROPERTIES OF PERMALLOY FILMS BY SUBMICROMETER PATTERNING

We have measured shape-induced high frequency properties of patterned submicrometer Permalloy (Py) arrays. We sputtered and patterned Py films on gold (Au) transmission lines, using chromium (Cr) as adhesion layers for Au and Py deposition. Each Py bar in the arrays is 10 μm long and 100 nm thick. The widths of the Py bars in two different arrays are 240 and 550 nm, respectively. Micromagnetic simulations indicate single domain magnetization distribution in these Py structures. The measured ferromagnetic resonance frequencies without bias field are approximately 11.5 and 8 GHz, respectively. We obtained the corresponding susceptibilities. The experimental results agree with theoretical predictions.

II.1 Introduction

Incorporating ferromagnetic materials into integrated microwave devices is a promising approach for the development of on-chip high-performance circuit components, such as inductors [2.1-2.3], filters [2.4], and circulators [2.5]. These devices, especially inductors, are a bottleneck for system-on-chip (SOC) development. Unfortunately, the natural ferromagnetic resonance (FMR) frequencies, f_{FMR}, of ferromagnetic materials are low, mostly lower than a few gigahertz [2.6-2.7]. Furthermore, significant losses arise at frequencies far below FMR frequencies. The

losses are determined by the imaginary part of the permeability (μ''), which follows f_r^{-4} [2.8]. As a result, there have been many efforts to improve FMR frequencies. Exploiting shape anisotropy [2.4], [2.9-2.10] of metallic ferromagnetic thin films is one of the promising approaches that are compatible with the planar processes of complementary-metal-oxide-semiconductor (CMOS) technologies. Among the materials that have been tested, Py films have attracted much attention for radio-frequency (RF) integrated circuit (IC) applications. Nevertheless, only limited FMR frequency improvements have been demonstrated for Py films even though large aspect ratios were used [2.6], [2.9-2.12]. On the other hand, it was shown that Ni-Fe nanowires with small cross section areas have natural FMR frequencies around 20 GHz [2.13-2.14]. However, the fabrication process is not compatible with CMOS process. Therefore, it is of great interest to investigate the high frequency properties of planar nanometer Py structures that can boost the FMR frequencies to 10 GHz and beyond.

II.2 Experiment Arrangement

Patterned planar Py films with different aspect ratios are incorporated with gold (Au) transmission lines for high-frequency property studies. The Au lines are 1 mm long, 250 nm thick and 5 μm wide. The Py arrays have a length of 10 μm and thickness of 100 nm with respective widths of 240 nm and 550 nm for two different sample lines. Figure II.1 (a) shows a section of the fabricated structure with 550 nm Py width. Figure II.1 (b) shows the alignment of the patterned Py array, the Au line, and the measurement contact pad. The fabrication used fused silica substrate, standard e-beam lithography, sputtering,

and lift-off processes. Chromium adhesion layers with 5–10 nm thickness are used for gold and Py deposition. The space between two adjacent Py structures is 100 nm. Identical control lines and contact pads, which do not have Py arrays, are also fabricated to de-embed high-frequency parasitic effects. Full two-port calibrations were conducted before scattering parameter measurements. Parasitic effects from the measurement pads and gold lines are de-embedded in Py susceptibility extraction by use of the procedures in [2.15-2.16].

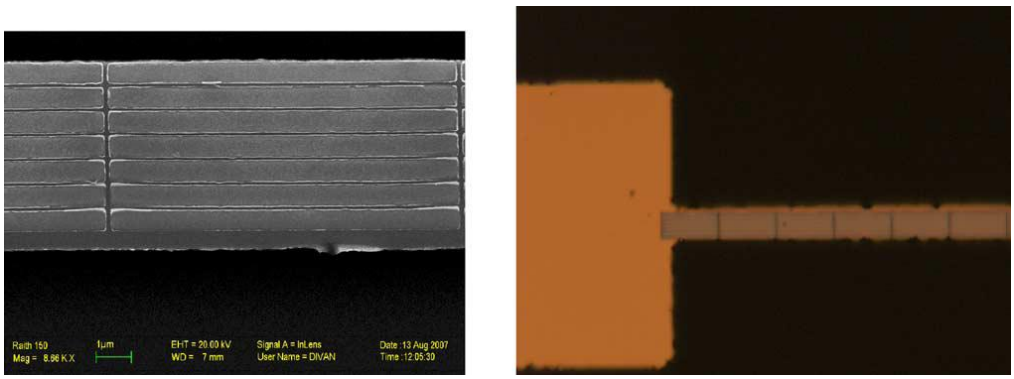

Figure II.1 (a) Scanning electron microscope picture of a fabricated Py array on an Au line. Each patterned Py structure is 550 nm wide. The space between two adjacent Py structures is 100 nm. (b) Optical micrograph.

II.3 Results and Discussions

Figure II.2(a) shows the measured scattering parameters (transmission coefficients, $|S_{21}|$) of the sample structures without bias field. A comparison between the control line and the sample lines show high FMR frequencies, 11.5 GHz for the 240 nm array, and 8 GHz for the 550 nm array. These frequencies are significantly higher than

5.3 GHz, which was previously published for planar Py structure that used shape anisotropy to boost the FMR frequency [2.11]. In addition, there is a transmission coefficient difference between the control line and the sample lines due to two reasons. First, the addition of Py arrays increases line inductance but keeps line capacitance virtually identical. This increases the high-frequency characteristic impedance. Secondly, no insulation layers are deposited between the Py films and the gold lines. As a result, the sample line is less resistive, resulting in less resistance, approximately 7% lower DC resistance in DC measurements. Therefore, the high-frequency signal attenuation coefficients, which are determined by line resistance R and characteristic impedance Z_0 through $\exp\left(-R/\left(2Z_0\right)\right)$, are smaller. Figure II.2(b) and Figure II.2(c) show the extracted susceptibility of the patterned Py films. Figure II.2(d) shows the FMR frequency shift upon applying a 50 mA external DC current. The shift qualitatively agrees with micromagnetic simulation analysis using the Object Oriented MicroMagnetic Framework (OOMMF) [2.17], which accounts for the tilting of the equilibrium angle of the magnetization due to the presence of a DC bias magnetic field. Similar phenomena were first observed in [2.12]. The shift mechanism will be discussed in the following chapter.

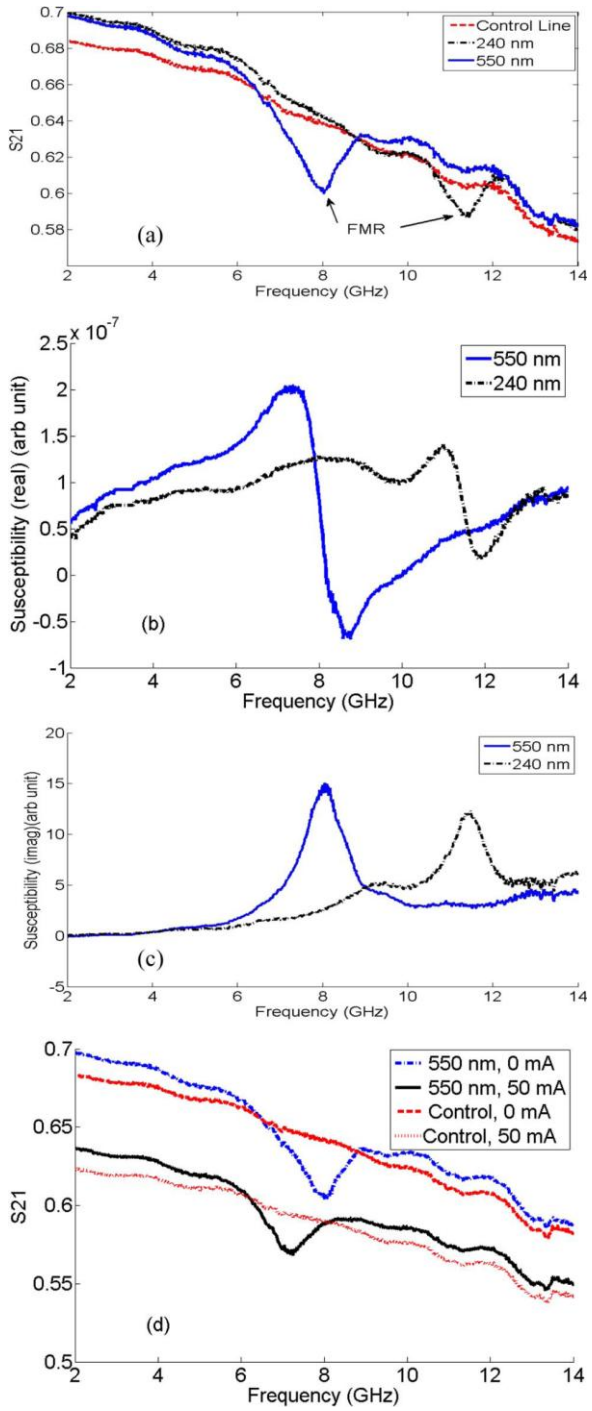

Figure II.2 (a) Signal transmission coefficients (S_{21}). (b) Measured susceptibility (real part). (c) Measured susceptibility (imaginary part). (d) FMR frequency shift when a 50 mA DC current is applied.

Figure II.3 shows the magnetization distribution of the 240 nm and 550 nm planar Py films obtained from OOMMF simulation, which reliably predicts magnetic domain configurations for these types of structures [2.18]. We expect essentially a single magnetic domain with negligible closure domain structures. Therefore, the magnetization dynamic processes that yield the properties in Figure II.2 are dominated by magnetization rotations. Furthermore, OOMMF simulations show that strong static and dynamic interactions between two adjacent Py bars occur only when their separation is around 20 nm or below. Therefore, we assume no strong couplings in the test samples, with each individual Py bar in the array behaving independently and identically. We can use Kittel equation to calculate the FMR frequencies for a single Py bar. The demagnetization factors can be calculated by using the equations in [2.19]. Fig. 4 shows the calculated FMR frequency for different Py widths. These material parameters are chosen to match the observed FMR frequencies for the 240 nm Py bar. The measured frequency for the 550 nm Py bar is lower than that from (1), even if a finite is introduced. Possible reasons for the deviation include the influence of the closure end domains (as seen in Figure II.3) and stronger dipolar coupling for the wider stripes, which may reduce the effective field. Nevertheless, Figure II.4 shows that the highest FMR frequency occurs when the long Py films have a square cross-section. It suggests a guideline for microwave device design and process development. The results also imply that FMR frequencies above 20 GHz can be obtained by use of ferromagnetic materials, such as FeCo, that have larger saturation magnetizations.

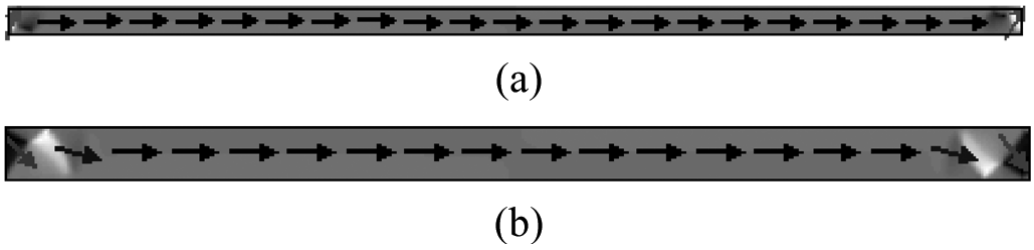

Figure II.3 Magnetization distributions of two individual Permalloy bars obtained from OOMMF simulation. The dimensions are (a) 240 nm × 10 μm × 100 nm (b) 550 nm × 10 μm × 100 nm.

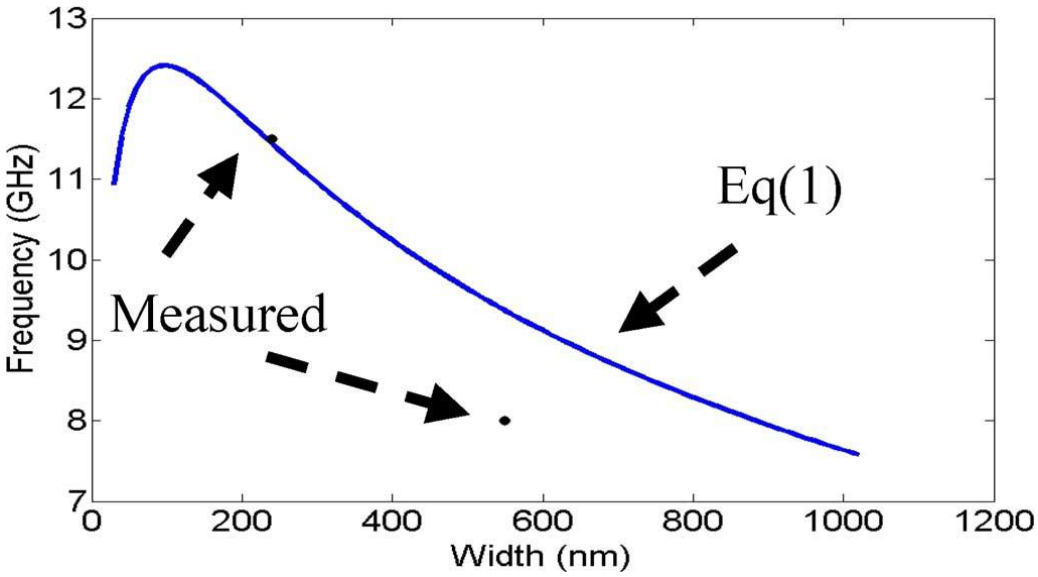

Figure II.4 FMR frequencies for different Py bar widths. The two dots indicate the measured frequencies.

The high-frequency susceptibility of the Py structures, when measured perpendicular to the easy axis and in the film plane, can be obtained from (2) in [2.20]

$$\chi(\omega) = \frac{4\pi M_s \gamma^2 \left(j\omega\alpha/\gamma + 4\pi M_s N_z \right)}{\omega^2 - j\left(2H_k + 4\pi M_s \left(1 - N_x\right)\right)\omega\alpha\gamma - \omega_f^2} \tag{II.1}$$

where α is the damping parameter. Figure II.5 shows the obtained susceptibility for the Py samples with $\alpha = 0.021$. The 550 nm Py film has higher susceptibility, but lower FMR frequency, consistent with the measured results in Figure II.2. Theoretical susceptibility ratios (both real and imaginary part) are close to that from measured data for frequencies below 7.5 GHz. The ratios are taking between the susceptibilities of the two different samples. Clearly, Figure II. 2 and Figure II. 5 show a tradeoff between FMR frequency and permeability when these films are used for microwave device developments, as discussed in the theoretical work in [2.21-2.23]. The FMR linewidth in Figure II.2 is larger than that in Figure II.5. Possible reasons for the linewidth broadening include sample inhomogeneities between different stripes (i.e., slightly different thickness, width, roughness), spin-pumping into the underlying chromium adhesion layer and gold layer (since there is no underlying insulating layer), some small residual dipolar coupling. Nevertheless, the linewidth broadening is comparable or better than those in previously published work, such as that in Fig. 2 of [2.11]. The broadening will limit the highest operating frequency for some applications, such as inductors. But it may not be a big concern for other applications, such as low-pass filters.

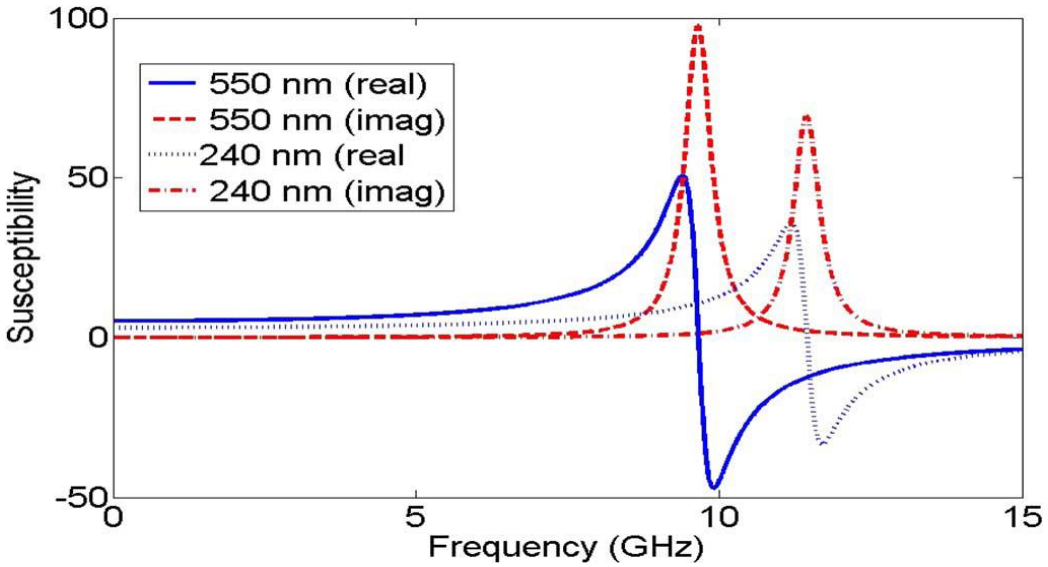

Figure II.5 Calculated susceptibility of the patterned Py films.

II.4 Conclusions

We demonstrated the feasibility of tailoring high frequency properties via suitable patterning of Py films. Py submicron structures are obtained and characterized through scattering parameter measurements. OOMMF simulations show single domain magnetization distribution in each Py structure. The obtained FMR frequencies are 11.5 GHz and 8 GHz for 240 nm and 550 nm Py films, respectively. Further analysis shows that square cross section nano-films exhibit the highest FMR frequency.

References

[2.1] Y. Zhuang, B. Rejaei, E. Boellaard, M. Vroubel, and J. N. Burghartz, "Integrated Solenoid Inductors with Patterned Sputter-deposited Cr/Fe10Co90/Cr Ferromagnetic Cores," *IEEE Electron Device Lett.* **24**, 224 (2003).

[2.2] J. Kim, W. Ni, C. Lee, E. C. Kan, I. D. Hosein, Y. Song, and C. Liddell, "Magnetic Property Characterization of Magnetite (Fe3O4) Nanorod Cores for Integrated Solenoid RF Inductors," *J. Appl. Phys.* **99**, 08R903 (2006).

[2.3] Y. Zhuang, B. Rejaei, E. Boellaard, M. Vroubel, and J. N. Burghartz, "GHz Bandstop Microstrip Filter Using Patterned $Ni_{78}Fe_{22}$ Ferromagnetic Film," *IEEE Microw. Wireless Compon. Lett.* **12**, 473 (2002).

[2.4] Y. V. Khivintsev, B. K. Kuanr, I. Harward, R. E. Camley, and Z. Celinski, "Iron-based Microstrip Band-stop Filters at High Microwave Frequency Range: Design Optimization Using Shape Anisotropy," *J.Appl. Phys.* **99**, 08P512 (2006).

[2.5] A. Saib, M. Darques, L. Piraux, D. Vanhoenacker-Janvier, and I. Huynen, "Unbiased Microwave Circulator Based on Ferromagnetic Nanowires Arrays of Tunable Magnetization State," *J. Phys. D: Appl. Phys.* **38**, 2759 (2005).

[2.6] M. Vroubel, Y. Zhuang, B. Rejaei, J. N. Burghartz, A. M. Crawford, and S.Wang, "Calculation of Shape Anisotropy for Micropatterned Thin Fe-Ni Films for On-Chip RF Applications," *IEEE Trans. Magn.* **40**, 2835 (2004).

[2.7] A. M. Crawford, D. Gardner, and S. X. Wang, "High-frequency Microinductors with Amorphous Magnetic Ground Planes," *IEEE Trans. Magn.* **38**, 3168, (2002).

[2.8] B. Lax and K. J. Button, *Microwave Ferrites and Ferrimagnetics*. New York: McGraw-Hill, 1962.

[2.9] M. Vroubel, Y. Zhuang, B. Rejaei, J. N. Burghartz, A. M. Crawford, and S. X. Wang, "Calculation of Shape Anisotropy for Micropatterned Thin Fe-Ni films for On-Chip RF Applications," *IEEE Trans. Magn.* **40**, 2835 (2004).

[2.10] B. Kuanr, R. E. Camley, and Z. Celinski, "Effect of Shape Anisotropy on Stop-Band Response of Fe and Permalloy Based Tunable Microstrip Filters," *IEEE Trans. Magn.* **40**, 2841 (2004).

[2.11] Y. Zhuang, M. Vroubel, B. Rejaei, and J. N. Burghartz, "Shape-induced Ultrahigh Magnetic Anisotropy and ferromagnetic Resonance Frequency of Micropatterned Thin Permalloy Films," *J. Appl. Phys.* **99**, 08C705 (2006).

[2.12] T. Korn, M. Kerekes, U. Ebels, D. Stanescu, and P. Xavier, "Pumping Field-Induced Dynamic Effects in Micron-Sized Permalloy Lines and Their Influence on HF filter Applications," *IEEE Trans. Magn.* **41**, 3514 (2005).

[2.13] A. Saib, M. Darques, L. Piraux, D. Vanhoenacker-Janvier, and I. Huynen, "An Unbiased Integrated Microstrip Circulator Based on Magnetic Nanowired Substrate," *IEEE Trans. Microw. Theory Tech.* **53**, 2043 (2005).

[2.14] G. Goglio, S. Pignard, A. Radulescu, L. Piraux, I. Huynen, D. Vanhoenacker, and A. V. Vorst, "Microwave Properties of Metallic Nanowires," *Appl. Phys. Lett.* **75**, 1769 (1999).

[2.15] C. Chen and M. J. Deen, "A General Noise and S-parameter Deembedding Procedure for On-Wafer High-Frequency Noise Measurements of MOSFETs," *IEEE Trans. Microw. Theory Tech.* **49**, 1004 (2001).

[2.16] P.Wang, W. Ni, N. C. Tien, and E. C. Kan, "High-frequency Permalloy Permeability Extracted from Scattering Parameters," *J. Appl. Phys.* **95**, 7034 (2004).

[2.17] M. Donahue and D. Porter, The Object Oriented MicroMagnetic Framework (OOMMF) Project at ITL/NIST [Online]. Available: http://math.nist.gov/oommf/ 2004

[2.18] S. Azeemuddin, A. Hoffmann, R. Divan, M. Donahue, S. H. Chung, and P.Wang, "High-frequency, Domain-wall Motion and magnetization Rotation of Patterned Permalloy Films under External Magnetic Field Excitation," in *IEEE NANO 2006*,853 (2006).

[2.19] A. Aharoni, "Demagnetizing Factors for Rectangular Ferromagnetic Prisms," *J. Appl. Phys.* **83**, 3432 (1998).

[2.20] O. Gerardin, J. B. Youssef, H. L. Gall, N. Vukadinovic, P. M. Jacueart, and M. J. Donahue, "Micromagnetics of the Dynamic Susceptibility for Coupled Permalloy Strips," *J. Appl. Phys.* **88**, 5899 (2000).

[2.21] N. A. Buznikov, A. L. Rakhmanov, and K. N. Rozanov, "Dynamic Permeability of Ferromagnetic Thin Films with Stripe Domain Structure," *IEEE Trans. Magn.* **38**, 3123 (2002).

[2.22] R. M.Walser,W.Win, and P. M. Valanju, "Shape-optimized Ferromagnetic Particles with Maximum Theoretical Microwave Susceptibility," *IEEE Trans. Magn.* **34**, 1390 (1998).

[2.23] G. Perrin, O. Acher, J. C. Peuzin, and N. Vukadinovic, "Sum Rules for Gyromagnetic Permeability of Ferromagnetic Thin Films: Theoretical and Experimental Results," *J. Magn. Magn. Mater.* **157**/**158**, 289 (1996).

CHAPTER THREE

DIRECT CURRENT EFFECTS ON HIGH-FREQUENCY PROPERTIES OF PATTERNED PERMALLOY THIN FILMS

DC current effects on high-frequency properties of two different Permalloy (Py) submicron patterns of 0.24 μm and 0.55 μm width, 10 μm length and 100 nm thickness are investigated experimentally. The natural ferromagnetic resonance (FMR) frequencies for the two samples are ~ 8.5 and 11.5 GHz. A 50 mA DC current results for both samples in a FMR frequency reduction of about 1 GHz. In addition susceptibility spectra for the samples are extracted from the measurement data. Effects of magnetic fields generated from external magnets on the submicron patterns were also tested for comparison. To obtain the same magnetization rotation angle, the external magnetic field needs to be about five times larger than the Ampere's field created by the DC current. This behavior is unique and may be associated with the increased thermal energy from the Joule heating effects.

III.1 Introduction

DC currents often flow through these RF devices in a circuit or system. For example, bias DC currents up to tens of milliamps pass through the inductors when they are used for tuning circuits or bias circuits of amplifiers (such as the RF choke inductor of an amplifier). The DC currents will introduce Ampere's fields and Joule heating effects, which will cause RF property changes in the patterned ferromagnetic materials. For instance, it has been reported that temperature variations and high magnitude pumping fields can cause unexpected shifts in patterned magnetic materials [3.1-3.2]. Furthermore,

temperature change and Ampere's fields could come from other circuit components. As a result, the RF device characteristics would change accordingly, so would the circuit and system performances.

Patterned magnetic materials could be more prone to these current induced effects due to their decreased volume. Such effects may pose a fundamental limit on the application of these materials. Therefore, it is of great interest to understand these effects. In this chapter, the DC current effects on the high-frequency properties of submicron Permalloy (Py) thin films are studied. Section III.2 describes the test samples and measurement approaches. Section III.3 presents the observed f_{FMR} shifts of the Py embedded transmission lines. Section III.4 concludes the chapter.

III.2 Experiment Arrangement

A broadband microwave coplanar waveguide (CPW) transmission line method was used to study DC current effects on high-frequency properties of the patterned Py thin films. The sample fabrication process has been discussed in Chapter 1. Figure III.1 (a) shows a scanning electron microscope (SEM) picture of a section of Au line with 0.24 μm samples. These large aspect ratios are chosen for the Py patterns to ensure that single domains are the dominant remanent states [3.3]. A vector network analyzer (VNA) was used to supply a microwave signal and to measure the transmission and reflection coefficients. Full two-port calibration was conducted before the measurements. Two types of experiment were performed: one with DC currents passing through the transmission line, illustrated in the top of Figure III. 1(b); the other with an external

magnetic field from magnets, shown in the bottom of Figure III. 1(b). All the measurements were conducted with arrays of patterned Py films at room temperature.

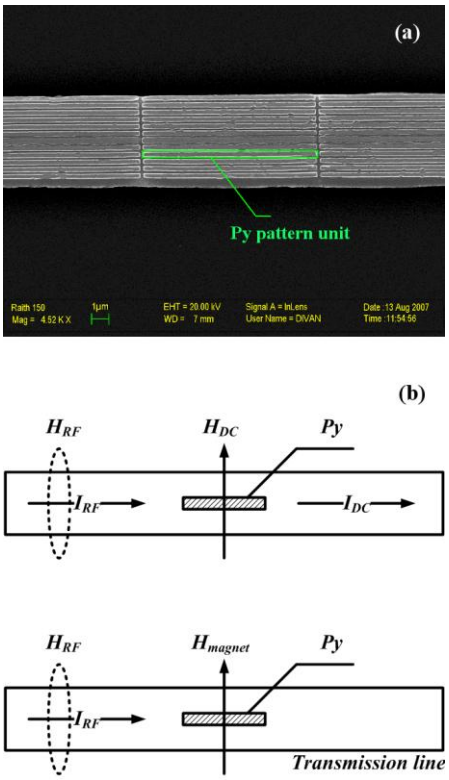

Figure III.1 (a) Scanning electron microscope picture of a fabricated 0.24 μm Py array on an Au line. One Py wire is framed in the picture to illustrate the Py position. (b) Illustration of measurement setup. Top: DC current applied only, Bottom: External magnetic field applied only. H_{DC} stands for the Ampere's field produced by the DC current, H_{magnet} stands for the external magnetic field and H_{RF} stands for the RF magnetic field produced by the RF field.

III.3 Results and Discussions

Figure III. 2(a) shows the measured scattering parameters (transmission coefficient, $|S_{21}|$) of the tested Py arrays without DC currents or external magnetic fields. The frequencies showing peak absorptions correspond to the FMR frequencies of the submicron patterns under test. The FMR frequencies as a function of easy axis bias field are shown in Figure III. 2(b). The shape anisotropy fields, $H_k(0.24\ \mu m) = 107.5\ KA/m$ for the 0.24 μm wide Py film and $H_k(0.55\ \mu m) = 68.5\ KA/m$ for the 0.55 μm wide Py film, are extracted by fitting the data with the Kittel equation as in:

$$f_r = \frac{g \cdot \gamma}{4\pi}\sqrt{(H_{Bias} + H_{Ani})(M_s + H_{Bias} + H_{Ani})} \qquad \text{(III.1)}$$

where $4\pi M_s = 9\ kG$ is the saturation magnetizations, H_{Ani} is the shape anisotropy field, $g = 2.08$ is the Landé factor, $\gamma = 176\ GHz/T$ is the gyromagnetic ratio and H_{Bias} is the bias field. The estimated theoretical value of the shape anisotropy field is about twice the experimental extracted value. The discrepancy may come from the dipolar interactions between each wire. Further investigation of this issue is needed.

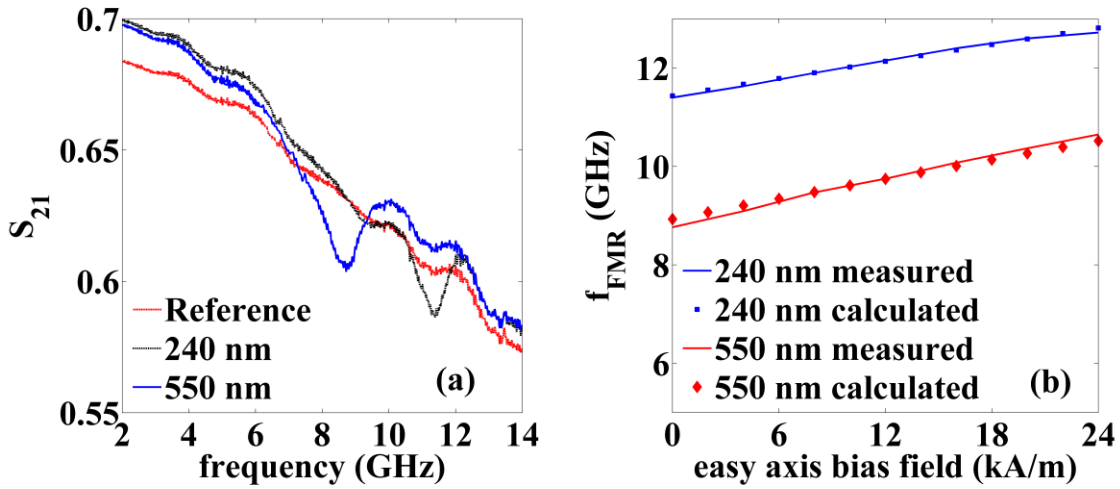

Figure III.2 (a) Measured transmission coefficients of the test samples and the reference transmission line that does not have Py thin films. (b) FMR frequency: easy-axis field dispersions for 0.24 μm and 0.55 μm Py patterns.

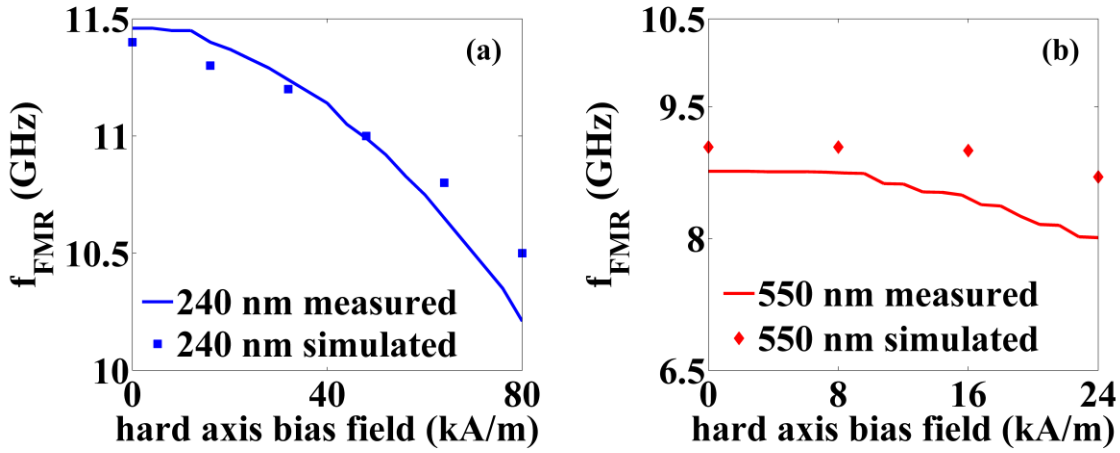

Figure III.3 FMR frequency: hard-axis field dispersions for (a) 0.24 μm and (b) 0.55 μm Py patterns.

Figure III. 3 shows the FMR frequencies as a function of external magnetic field applied along the hard axis direction. Here the in-plane rotation is given by the competition between the external field (rotating $\vec{M}$ perpendicular to the wire axis) and the anisotropy field (rotating $\vec{M}$ parallel to the wire axis) [3.4]. Thermal heating effects due to power absorption at FMR can be excluded because the thick Au transmission line underneath the Py pattern provides an efficient heat sink and the applied microwave power is only 0 dBm. The results agree with micromagnetic simulation results reasonably well. The simulations were performed using Objective Oriented Micromagnetic Framework (OOMMF) [3.5]. The static magnetization configurations for different bias fields were first obtained in all the OOMMF simulations. The susceptibility versus frequency plots are obtained by applying an exponentially decaying field pulse, $H_{pulse}(t) = H_0 \exp\left(-10^9 t\right)$, and recording the magnetization response as a function of time, the unit of time is in second. The complex susceptibility spectra are calculated by dividing the fast Fourier transform (FFT) of the hard axis averaged magnetization by the FFT of the applied pulse field. In the simulations, the cell size for both samples is 10 nm $\times$ 10 nm in lateral plane and 50 nm in thickness. The saturation magnetization is the same as that used in the Kittel equation calculations. The OOMMF simulated FMR frequencies correspond to the bulk mode of the samples. The discrepancy in the high field magnitude region of 0.55 μm Py is because the magnetization distribution of the wider Py becomes nonhomogeneous across the width of the film as $\vec{M}$ rotates towards the hard axis [3.6], and this was not taken account of in the simulation.

Easy axis bias was applied after applying hard axis bias field to saturate the samples along the easy axis. After that the easy bias was removed to let the Py pattern return to its remanent state. The scattering parameter data was used as a simple probe of the remanent state of the samples under test. As shown in Figure III. 1(a), the natural scattering parameters measured when there were no fields or currents applied were recorded as references. The DC current was not applied until the scattering parameters returned to the reference values. DC currents were then swept from 0 to 50 mA with the DC source connected to the VNA through a bias tee, and no external magnetic field was applied during the process. The FMR frequencies corresponding to different bias currents are shown in Figure III. 4(a). The FMR frequency shift values as a function of the bias current are shown in Figure III. 4(b). The maximum Ampere's fields associated with the DC currents can be estimated with Ampere's law $H_{DC} = I/2w$ [3.7- 3.8], where I is the DC current, w is the width of the central line of the CPW. The value of $H_{DC} = I/2w$should be a good approximation for the Ampere's field across the sample since the magnitude of the field interacting with the material under test is within 90% to 100% of this value. The corresponding Ampere's fields of the DC current are labeled on the top x-axis of Figure III. 4. The fields are along the hard axis direction of the patterned Py films. By comparing Figure III. 3 and Figure III. 4, it is clear that FMR frequency shifts follow the similar trends, but for the same amount of FMR frequency shift the required Ampere's field intensity is much smaller. This indicates that the FMR frequency shifts in the two experiment setups are caused by different mechanisms.

In the DC current case both the Ampere's fields and Joule heating effects should be considered. We attribute the FMR shift predominantly to the Joule heating effects because the maximum Ampere's field is only 5 kA/m. Thermal effects, such as the thermal energy enhanced augmentation of magnetization rotation, domain reconfiguration [3.9], and domain wall depinning [3.10] will induce domains and make it easier to tilt the magnetization direction away from the easy axis, which in turn cause the reduction of the FMR frequency. One reason for the FMR frequency reduction is that temperature increase due to Joule heating effects can decrease the material's magnetic moment: saturation magnetization M_s and anisotropy field H_{ani}. The temperature change can be estimated from the resistance change of the Au transmission line [3.11]. The line resistance, taken concurrently with the scattering parameters, increased from 43.1 Ω to 63.5 Ω when the DC current is swept from 0 to 50 mA. The corresponding temperature change of $\Delta T = 140\ ^\circ\mathrm{C}$ is obtained from the equation $R = R_0\left[1+\beta\left(T-T_0\right)\right]$, where R and R_0 are the final and initial resistance of the Au line, T and T_0 are the final and initial temperature, $\beta = 3.4\times10^{-3}/\ ^\circ\mathrm{C}$ is the temperature coefficient of resistivity of Au. The decrease of the in-plane anisotropy of about 10 kA/m for the 0.24 μm wide Py films and 6 kA/m for the 0.55 μm wide Py films can be obtained from Bloch's $T^{3/2}$ relation i.e., $M_s\left(T\right) = M_s\left(0\right)\left(1-AT^{3/2}\right)$ where the coefficient A is material dependent [3.1], [3.12]. Temperature dependence of $M_s(T)$ was later taken into account in the OOMMF simulations. $H_{ani}(T)$ has also been considered since the temperature dependence of the anisotropy should just come from the temperature dependence of the saturation

magnetization, since the demagnetizing factors just depend on the geometry. Simulation result shows that the FMR frequency reduced by about 0.38 GHz for the 550 nm stripe at 50 mA DC current. Meanwhile the measured value is 0.8 GHz. This difference implies that other than the reduction of the magnetic moment, effects such as the domain wall depinning which were not considered in the simulation also play an important role in the FMR reduction.

Even though the observation is not fully understood, we simplified the problem by assuming the samples keep uniform magnetization during the precession in both experimental setups. Then the FMR shift is only caused by the magnetization rotation. The equilibrium angle, which is no longer parallel to the easy axis, is chosen to be an indicator; it can be calculated from the ratio of hard and easy axis projections of the tilted magnetization. The simplified uniform magnetization model and experimental data show that for the 0.55 μm samples the Ampere's field needed to obtain the same equilibrium angle is about 5 times less than does the external magnetic field, as shown in Figure III. 5. This should be essentially caused by the assistance of the thermal effects from the Joule heating effects. The observed phenomena imply that applying DC current could be a potential candidate for the enhancement of microwave-assisted magnetic switching, which is drawing more and more interest in magnetoelectronics researches [3.13- 3.16].

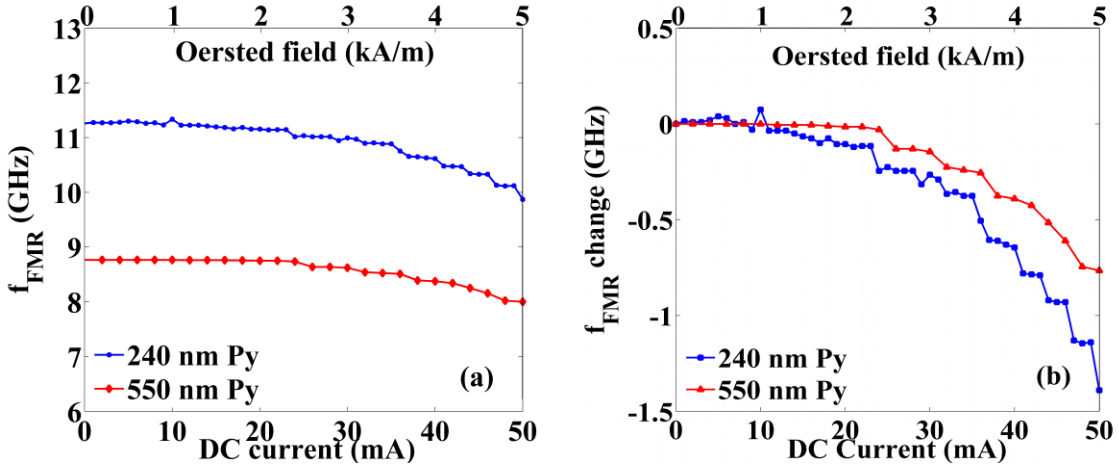

Figure III.4 (a) FMR frequency: current dispersions for 0.24 μm and 0.55 μm Py patterns. (b) The FMR frequency shifts with respect to their zero bias f_{FMR} as a function of the bias current.

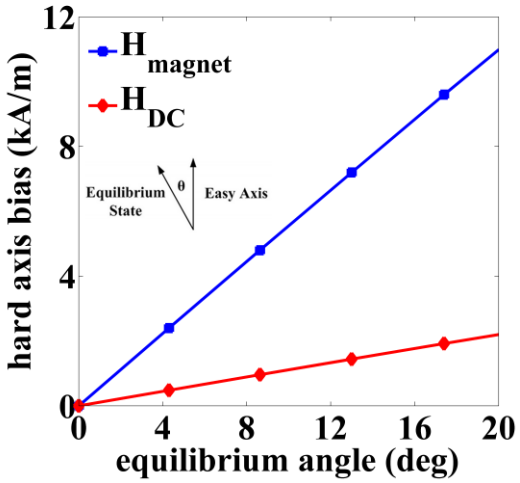

Figure III.5 Comparison between simulated equilibrium angles induced by Ampere's and external magnetic fields.

The susceptibility spectra are extracted by using the measured FMR frequencies and equation (2) in [3.24]:

$$\chi(\omega) = \frac{4\pi M_s \gamma^2 \left(j\omega\alpha/\gamma + 4\pi M_s N_z \right)}{\omega^2 - j\left(2H_k + 4\pi M_s \left(1 - N_x\right)\right)\omega\alpha\gamma - \omega_f^2} \tag{III.2}$$

where α is the damping constant, ω_f is the measured FMR angle frequency, H_k is the magnetocrystalline anisotropy field, N_x and N_z are the demagnetization factors in the sample length and thickness directions. Since the fabricated Py structures are rectangular prisms, their demagnetization factors can be calculated by using the equations in [3.25]. A value of $\alpha = 0.02$ is used in our calculation according to [3.9], [3.26-3.27]. The calculated real part of susceptibility as a function of DC current and frequency are shown in Figure III. 6 (a) and (b). It is shown that in the frequency range below the FMR frequency the variation of susceptibility with respect to bias current is significant, especially at the frequencies close to f_{FMR}. The variation reaches the maximum at the FMR frequency. The calculated real part of susceptibility as a function of external magnetic field and frequency are shown in Figure III. 6 (c) and (d). It shows that a much stronger external magnetic field is needed to get the same level of susceptibility variation. The imaginary part of the susceptibility is not shown here since the values are near zero and do not change much when the frequency is below FMR frequencies.

The inductances of the Py embedded straight transmission lines in different DC current conditions are extracted from the admittance matrix of the two-port network converted from the measured scattering parameters with the equation:

$$L = \omega^{-1} \cdot \mathrm{Im}\left(1/Y_{11}\right) \qquad \text{(III.2)}$$

where Y_{11} is the first component of the admittance matrix. The inductance is affected by changes of both the imaginary and real part of the sample susceptibility. The changes of the imaginary part relating to the FMR frequency reductions affect the operational frequency range of the inductors since the inductors only work properly below the FMR frequency. The inductances of Py embedded transmission are drawn in Figure III. 7, it shows that the operational frequencies decreased by 9 and 12.5 percent for 0.24 μm and 0.55 μm Py embedded transmission lines, respectively, when a 50 mA DC current is applied. To investigate the effects of the Py thin film susceptibility real part variation on the inductances, the inductance increase in the operational frequency range are evaluated from the measured inductances by subtracting the reference value of the reference transmission line. The results are shown in Figure III. 8, it is seen that the inductance boost is increased by a factor of two as the DC current increased from 0 mA to 50 mA. This is in line with the susceptibility change shown in Figure III. 6. In practical circuit applications, this will make the inductance deviate from its designed value and further affect the circuit performances. The effects observed above would be more serious when more Py materials, such as in the stacked multiple layer structures, are embedded.

It is also shown in Figure III. 7 that the mean values of the transmission line inductances in the operational frequency range dropped by about 10 percent when a 50 mA DC current is applied. This decrease does not come from the ferromagnetic material property change because it also exists when comparing the inductances of the reference transmission line which does not have magnetic materials. The pronounced reduction of

the inductance at 50 mA is because the current redistribution in the cross section of the transmission lines. Since temperature change is proportional to the square of the current magnitude, it increases much quicker when higher currents are applied. At higher temperatures, the conductivity decrease of the transmission line causes metal skin depth increase. This in turn varies the current distribution in the cross section of the Au transmission line. The current will distribute more uniformly cross the transmission line which is analogous to that more inductors are in parallel and that will cause the total inductance value to decrease.

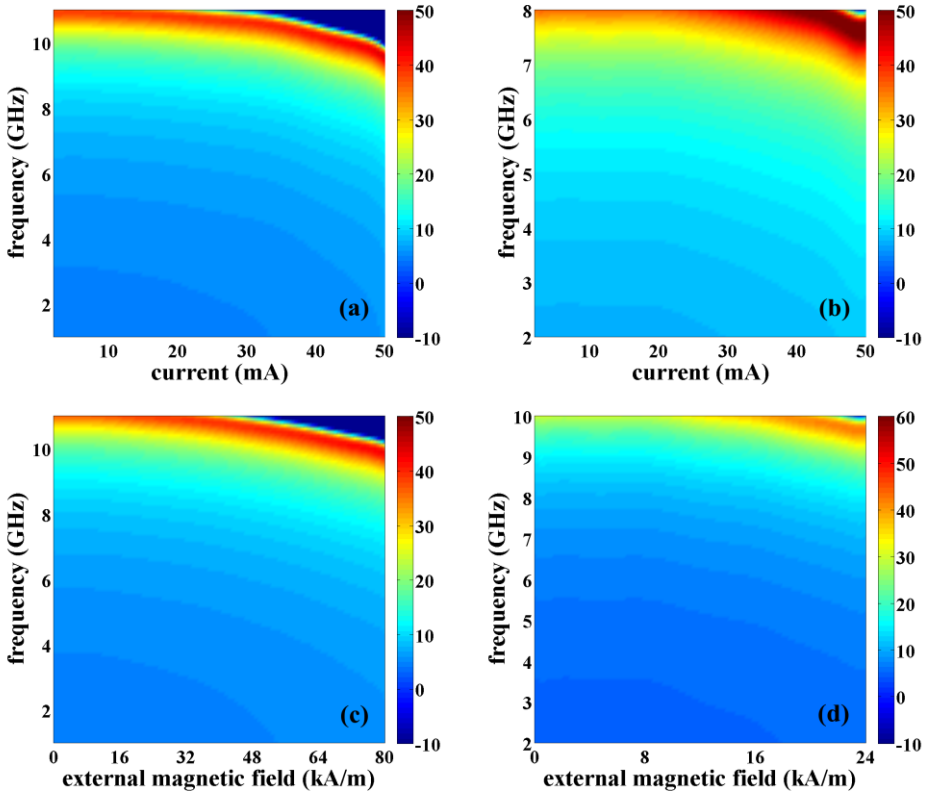

Figure III.6 Extracted susceptibility spectrum for (a) 0.24 μm and (b) 0.55 μm Py as a function of DC current and frequency; and as a function of external magnetic field and frequency (c) 0.24 μm and (d) 0.55 μm Py.

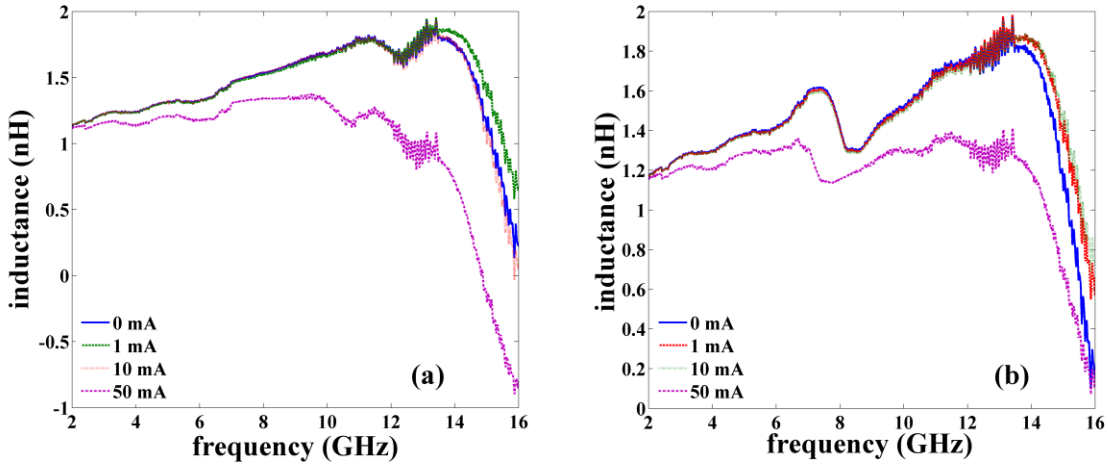

Figure III.7 Inductances versus frequency for different DC currents for (a) 0.24 μm and (b) 0.55 μm Py.

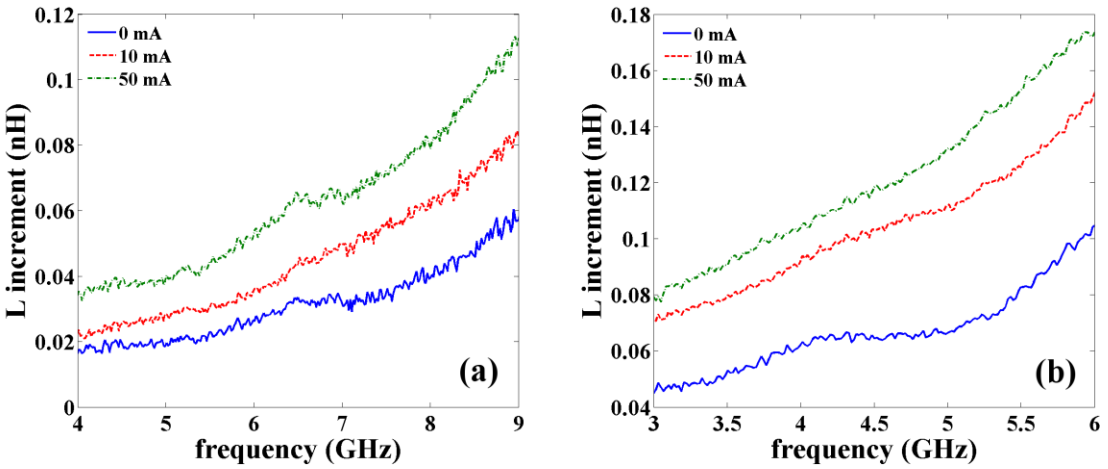

Figure III.8 Inductance increases versus frequency for different DC currents for (a) 0.24 μm and (b) 0.55 μm Py.

III.4 Conclusions

DC current effects on RF properties of submicron-sized Py patterns were experimentally investigated. It is observed that the FMR frequency changes more sensitively to the DC current than to the external magnetic fields. To obtain the same FMR frequency reduction, the Ampere's field needed is only about 20 percent the magnitude of the external magnetic field. We attribute this unique phenomenon to the increased thermal energy level from the Joule heating effects. The susceptibility spectra and the inductance variations of Py embedded transmission lines for different DC levels will be further studied and discussed in the dissertation.

References

[3.1] S. X. Wang, N. X. Sun, M. Yamaguchi, and S. Yabukami, "Sandwich films: Properties of a new soft magnetic material," *Nature.* **407**, 150 (2000).

[3.2] X. Chen, Y. G. Ma and C. K. Ong, "Magnetic anisotropy and resonance frequency of patterned soft magnetic strips," *J. Appl. Phys.* **104**, 013921 (2008).

[3.3] B. K. Kuanr, R. Lopusnik, L. M. Malkinski, M. Wenger, M. Yu, D. Scherer II, R. E. Camley and Z. Celinski, "High-frequency characterization of Permalloy nanosized strips using network analyzer ferromagnetic resonance," *J. Appl. Phys.* **103**, 07C508 (2008).

[3.4] H. Zhang, C. Song, R. Divan, A. Hoffmann and P. Wang, "High-Frequency Properties of Permalloy Nanowire Arrays for RF Devices," *Nanotechnology 8th IEEE Conference on*, 621 (2008).

[3.5] J. Salvia, J. A. Bian and C. P. Yue, "Tunable on-chip inductors up to 5 GHz using patterned permalloy laminations," *IEDM Technical Digest. IEEE International.* 943 (2005).

[3.6] B. Kuanr, Z. Celinski, and R. E. Camley, "Tunable high-frequency band-stop magnetic filters," *Appl. Phys. Lett.* **83**, 3969 (2003).

[3.7] J. W. Wang, S.D. Yoon, V.G. Harris, C. Vittoria, and N.X. Sun, "Integrated metal magnetic film coupled line circulators for monolithic microwave integrated circuits" *Electron. Lett.* **43**, 292 (2007).

[3.8] N. Stutzke, S. L. Burkett and S. E. Russek, "Temperature and field dependence of high-frequency magnetic noise in spin valve devices," *Appl. Phys. Lett.* **82**, 91 (2003).

[3.9] T. Korn, M. Kerekes, U. Ebels, D. Stanescu, and P. Xavier, "Pumping-field-induced dynamic effects in micron-sized permalloy lines and their influence on HF filter applications," *IEEE Trans. Magn.* **41**, 3514 (2005).

[3.10] P. Wang, H. Zhang, R. Divan and A. Hoffmann, "Tailoring high-frequency properties of permalloy films via submicron patterning," *IEEE Trans. Magn.* **45**, 71 (2009).

[3.11] M. Moralejo, F. J. Castaño, C. Redondo, R. Ji, K. Nielsch, C. A. Ross, and F. Castaño, "Fabrication and magnetic properties of hexagonal arrays of NiFe elongated nanomagnets," *J. Magn. Magn. Mater.* **316**, e44 (2007).

[3.12] M. J. Donahue and D.G. Porter, OOMMF User's Guide, Version 1.0, National Institute of Standards and Technology, Gaithersburg, MD (Sept 1999).

[3.13] M. Bailleul, D. Olligs, and C. Fermon, "Micromagnetic Phase Transitions and Spin Wave Excitations in a Ferromagnetic Stripe," *Phys. Rev. Lett.* **91** 137204 (2003).

[3.14] T. J. Silva, C. S. Lee, T. M. Crawford, and C. T. Rogers, "Inductive measurement of ultrafast magnetization dynamics in thin-film Permalloy," *J. Appl. Phys.* **85** 7849 (1999).

[3.15] A. Yamaguchi, K. Motoi, "Broadband ferromagnetic resonance of Ni81Fe19 wires using a rectifying effect," *Phys. Rev. B.* **78**, 104401 (2008).

[3.16] R. H. Koch, G. Grinstein, G. A. Keefe, Yu Lu, P. L. Trouilloud, W. J. Gallagher and S. S. P. Parkin, "Thermally Assisted Magnetization Reversal in Submicron-Sized Magnetic Thin Films," *Phys. Rev. Lett.* **84**, 5419 (2000).

[3.17] D. IIgaz, M. Kläui, L, Heyne, O. Boulle, F. Zinser, S. Krzyk, M. Fonin, U. Rüdiger, D. Backes, and L. J. Heyderman, "Selective domain wall depinning by localized Oersted fields and Joule heating," *Appl. Phys. Lett.* **93**, 132503 (2008).

[3.18] K. Kim, J. Lee, S. Choe, and K. Shin, "Joule heating in ferromagnetic nanowires: Prediction and observation," *Appl. Phys. Lett.* **92**, 192509 (2008).

[3.19] C. M. Fu, P. C. Kao, H. S. Hsu, Y. C. Cao, C. C. Yu and J. C. A. Huang, "Temperature variation of step-induced anisotropy in Permalloy thin film grown on Mo stepped surface," *IEEE Trans. Magn.*, **38**, 2667 (2002).

[3.20] Y. Nozaki, K. Tateishi, S. Taharazako, M. Ohta, S. Yoshimura, and K. Matsuyama, "Microwave-assisted magnetization reversal in 0.36-μm-wide Permalloy wires," *Appl. Phys. Lett.* **91**, 122505 (2007).

[3.21] T. Moriyama, R. Cao, J. Q. Xiao, J. Lu, X. R. Wang, Q. Wen and H. W. Zhang, "Microwave-assisted magnetization switching of Ni80Fe20 in magnetic tunnel junctions," *Appl. Phys. Lett.*, **90**, 152503 (2007).

[3.22] G. Woltersdorf, C. H. Back, "Microwave Assisted Switching of Single Domain Ni80Fe20 Elements," *Phys. Rev. Lett.* **99**, 227207 (2007).

[3.23] C. Thirion, W. Wernsdorfer, and D. Mailly, "Switching of magnetization by nonlinear resonance studied in single nanoparticles," *Nat. Mater.* **2**, 524 (2003).

[3.24] O. Gerardin, J. B. Youssef, H. L. Gall, N. Vukadinovic, P. M. Jacueart, and M. J. Donahue, "Micromagnetics of the dynamic susceptibility for coupled Permalloy stripes," *J. Appl. Phys.* **88**, 5899 (2000).

[3.25] Aharoni, "Demagnetizing factors for rectangular ferromagnetic prisms," *J. Appl. Phys.* **83**, 3432 (1998).

[3.26] S. E. Russek and S.Kaka, "Time and frequency domain measurements of ferromagnetic resonance in small spin-valve," *IEEE Trans. Magn.* **36**, 2560 (2000).

[3.27] H. Zhang and P. Wang, "A new method for high-frequency characterization of patterned ferromagnetic thin-films," *J. Appl. Phys.* **105,** 1 (2009).

CHAPTER FOUR

DIRECT CURRENT EFFECTS ON MAGNETIZATION REVERSAL PROPERTIES OF SUBMICRON-SIZE PERMALLOY PATTERNS DEVICES

Ferromagnetic resonance (FMR) spectroscopy is used to measure direct-current (DC current) effects on the magnetization reversal properties of submicron-sized lateral patterned magnetic material. The observed FMR frequency-field relationship shows that for both 240 nm and 550 nm wide Permalloy (Py) nanowires the coercivity is reduced by ~33% when a 50 mA DC current passes through the transmission line where the nanowires are incorporated. The temperature dependence of the coercivity has a $\sqrt{T}$ relationship which suggests the coherent rotation mode tendency in such 100 nm thick Py nanowires.

IV.1 Introduction

Magnetization reversal (i.e. switching) processes of patterned magnetic structures are of great interest for the understanding of fundamental spin dynamics and the development of magnetic devices, such as magnetoresistive random access memory (MRAM) and reconfigurable microwave filters [4.1-4.4]. Recent extensive investigations show that the reversal processes are significantly affected by temperature (i.e. thermally assisted switching) in addition to external microwave fields (i.e. microwave assisted switching), both are important for magnetoelectronic technology development [4.5-4.16]. Most of these studies focused on thin films (less than 50 nm thick with a thickness to width ratio less than 0.5), in which switching takes place through nucleation followed by

domain wall propagation [4.17- 4.18]. For thicker films, entangled coherent rotation and curling mode are considered to be dominant in the reversal process, which has only been studied with vibrating sample magnetometer (VSM) measurement at room temperature [4.17], [4.19-4.20]. Such thick films are important for high-performance microwave device (e.g. filters and inductors) development while magnetization reversal provides a promising approach for reconfigurable operations through pure electrical tuning [4.4], [4.21-4.23]. Previously, we studied DC current (i.e. combined Joule heating and Oersted field) effects on FMR frequency shifts of such thick films since DC currents may exist in practical application as bias currents of the circuits [4.21]. In this work, we investigate DC current effects on magnetization reversal processes in patterned thick films (Py, $Ni_{80}Fe_{20}$). FMR spectroscopy, which has been proposed for microwave assisted magnetization reversal (MAMR) studies recently [4.5-4.6], [4.14-4.16], is used to directly study the switching of submicron-sized, laterally patterned Py films.

IV.2 Experiment Arrangements

The magnetization reversal and the effects of DC currents on the switching behavior are studied with two patterned Py arrays consist of 240 nm and 550 nm wide individual structures, respectively. Each of the Py structure is ~ 100 nm thick and 10 μm long with ~100 nm gap between two adjacent Py strips. Each array has approximately 10^3 nominally identical elements. The Py is grown by DC magnetron sputtering on top of a 5 μm wide gold (Au) coplanar wave guide (CPW) transmission line on a fused silica wafer. Details of sample preparation are given in Ref. 1. The CPW is used to apply a radio-

frequency (RF) field along the hard axis of the Py patterns. The DC current also passes through the CPW during the measurement. A vector network analyzer is used to detect the microwave absorption caused by ferromagnetic resonance (FMR). Furthermore, the dependence of FMR frequencies on external magnetic field and DC current is extracted from the measured transmission coefficients. Figure IV.1 shows the measurement system schematic, a magnetic sample under test and a typical transmission coefficient (S_{21}) spectrum.

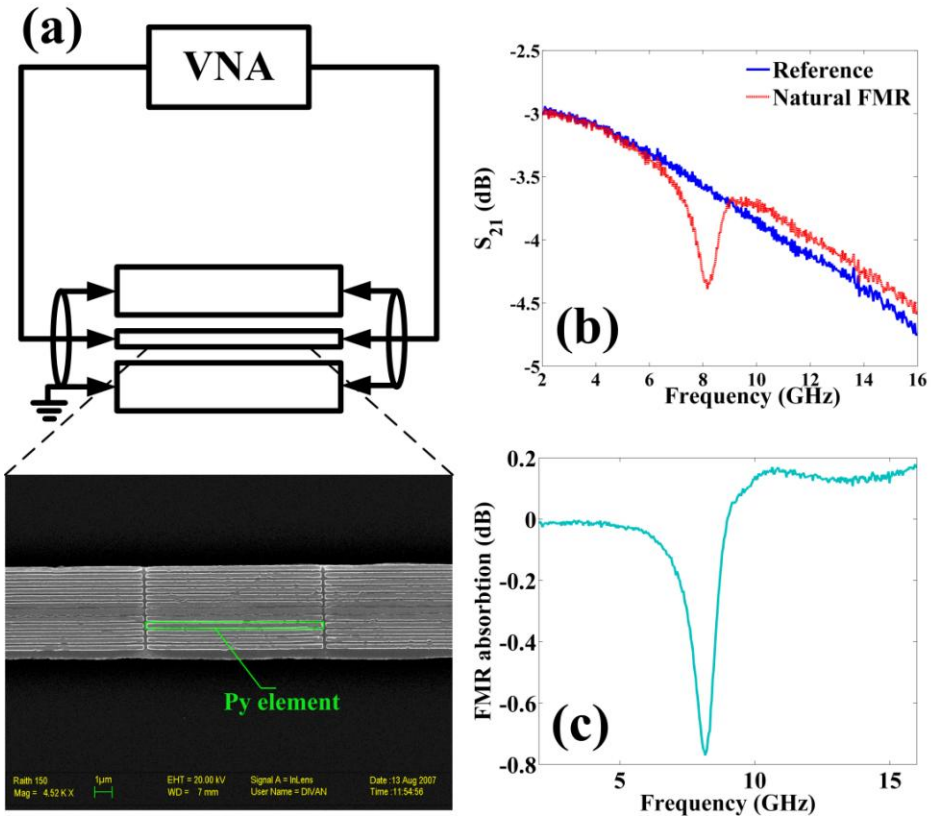

Figure IV.1 (a) Schematic of experiment setup and the magnetic sample under test. (b) A typical measured S_{21}. (c) The FMR absorption.

Magnetization reversal measurements were undertaken with the following steps: First, the magnetization was saturated along the easy axis of the patterns by applying a magnetic field H_s of 200 *mT*. This will set the magnetic configuration of the patterns to be a single domain and tune the sample FMR frequency beyond the measurement range. The measured transmission coefficient is used to be the reference for the subsequent measurements. Next the transmission coefficient spectrum is measured for different static fields swept from a relatively small starting field H_{st} ($\mu_0 H_{st} = 40mT$ for 240 nm pattern and $\mu_0 H_{st} = 20mT$ for 550 nm pattern), passing through zero, and then approaches $-H_{st}$. Then the field is increased from $-H_{st}$ to H_{st}. The reference signal and zero-field transmission signal of the 550 nm array are shown in Figure IV. 1(b). The reference signal is subtracted from the S_{21} measured at each static field. A typical result is shown in Figure IV. 1(c) with an absorption peak corresponding to the FMR. These peaks are recorded with respect to the static fields.

IV.3 Results and Discussions

Figure IV. 2 shows representative DC current effect data. The left and right column show 'FMR frequency hysteresis loops' corresponding to different DC currents: 10 mA, 30 mA and 50 mA for 240 nm and 550 nm Py patterns, respectively. The FMR frequency loop for zero DC current is not shown independently here because it has no visible difference compared with the 10 mA case. The vertical dashed lines in the figures show the field values where complete magnetization reversal occurs. Outside the dashed lines the data for decreasing and increasing fields overlap. This indicates that all the

magnetic patterns are switched to the same magnetization configuration. The data in these areas have good agreement with the Kittel's equation calculations which gives evidence that the magnetic patterns are of single domain configuration after a complete switching. As the width of the nanowires increases from 240 nm to 550 nm the natural coercivity of the Py elements decreases from ~24 *mT* to ~6 *mT*. A similar trend, i.e. the magnetization reversal field follow the inverse-width dependence, has been reported for lateral patterned magnetic elements in earlier studies with thin films [4.17], [4.24].

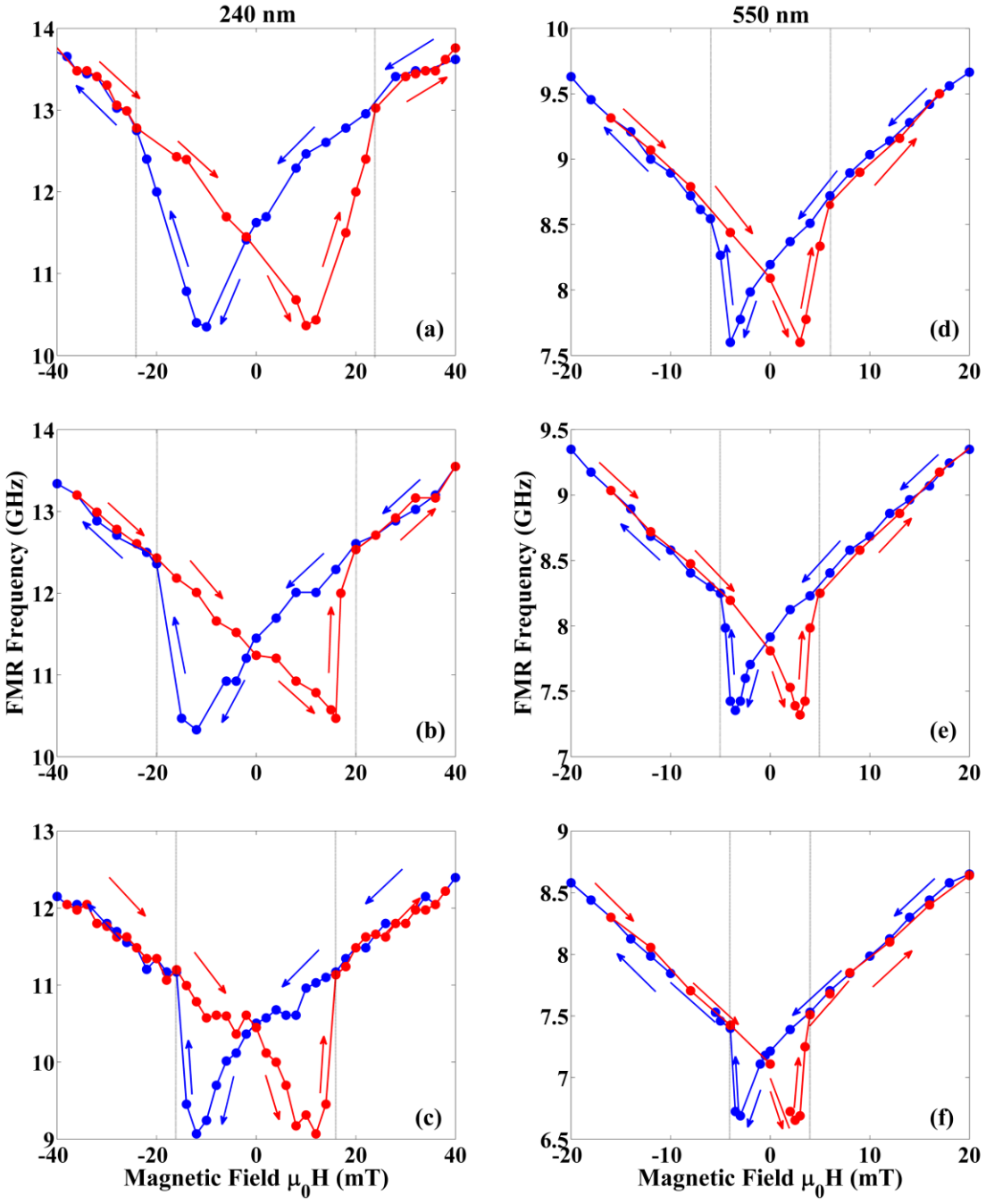

Figure IV.2 Left column: field dependence of FMR frequency for 140 nm array, (a) 0 and 10 mA. (b) 30 mA. (c) 50 mA. Right column: field dependence of FMR frequency for 140 nm array, (d) 0 and 10 mA. (e) 30 mA. (f) 50 mA.

The application of a DC current shows two effects. For both samples the dashed lines shift to lower fields regardless of the applied field direction. The shift depends on DC current density. For the 240 nm Py patterns the coercivity $\mu_0 H_{st} = 24\ mT$ is reduced to $16\ mT$ (a 33% reduction) with a 50 mA DC current. The coercivity of the 550 nm Py patterns reduced from $\mu_0 H_{st} = 6\ mT$ to $4\ mT$, the reduction is also 33%. This clearly demonstrates the high assisting efficiency of DC current to magnetization reversal. Also, FMR spectroscopy can be used to detect the magnetization reversal for submicron patterned magnetic materials. The other effect of the DC currents is that at zero-field the natural FMR frequencies of both samples are reduced by ~ 1 GHz when the current is increased to 50 mA. This agrees with our previous report [4.21].

A possible reason for the coercivity and nature frequency reductions would be the saturation magnetization variation as the temperature increases, which in turn changes the dominating shape anisotropy. The temperature is extracted from the measured resistance of the Au transmission line through $R = R_0\left[1+\alpha\left(T - T_0\right)\right]$, where α is the temperature coefficient [4.7]. The top panel of Figure IV. 3 shows the normalized coercivity and the temperature change as a function of the applied DC current. The calculated shape anisotropy reductions are ~ 8% for both samples. However, this is not enough to account for such a large switching field change (~33%). The orthogonal Oersted field associated with the DC current should play a role. As the Oersted field is increased to its maximum value of 6.25 *mT*, the effective external static magnetic field has a larger angle away from the easy axis of the samples. This corresponds to a coercivity reduction as demonstrated in Ref. 20.

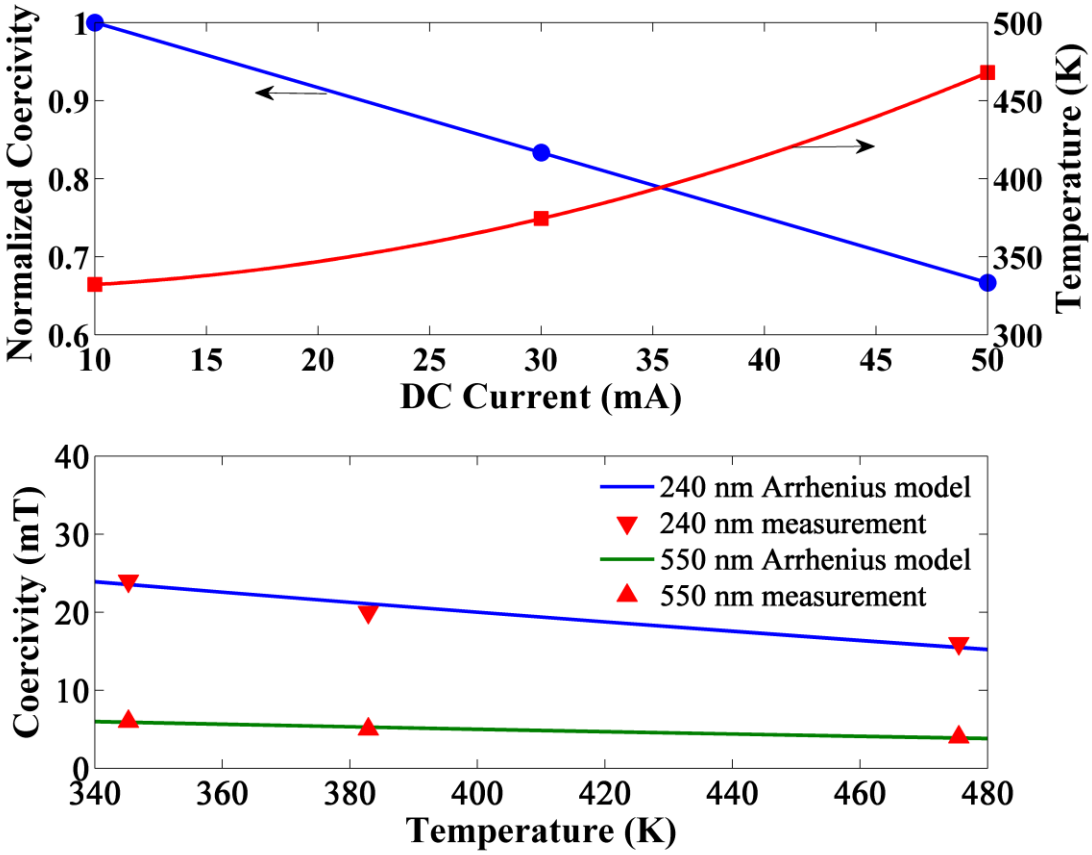

Figure IV.3 Top panel: DC current dependence of normalized coercivity and temperature. Bottom panel: comparison between the theoretical and measurement data for the temperature dependence of coercivity field.

The magnetization reversal mode is also explored in order to understand the reversal process. It is shown that the coercivity does not linearly depend on the temperature. This suggests that in our samples the reversal process no longer follows the nucleation mode as in thin films [4.18]. A general Arrhenius relationship for magnetization reversal probability, $P = f_0 \tau e^{-\Delta E / k_B T}$, can be used to model the switching

process [4.18], [4.25]. The energy barrier, ΔE, is shown to be proportional to the square of the magnetic field difference, i.e., $\Delta E = C\left(H_c^0 - H\right)^2$, for the samples of larger thicknesses. For a complete magnetization reversal, one can obtain the temperature dependence $H_c(T) = H_c^0\left[1-\left(k_B T\right)^{1/2}\ln\left(f_0\tau\right)/C\right]$, where f_0 is the attempt frequency (~1-10 GHz) and τ is the measurement time (in minutes), k_B is the Boltzmann constant, H_c^0 is the zero-temperature coercivity field, which can be estimated from the empirical equations in Ref. 18. The calculation results are in line with the measurement data, shown in the bottom panel of Figure IV. 3. Data fitting gives an extracted combined constant $\ln\left(f_0\tau\right)/C$ of 1.04×10^{-10} and H_c^0 of 70 mT and 17.5 mT for 240 nm and 550 nm patterns, respectively. This indicates that the switching process in our samples has a $\sqrt{T}$ temperature dependence, which usually occurs in coherent rotation mode. This is in line with previous report that the coherent rotation is present for field applied close to the easy axis of Py nanowires with an 80 nm thickness [4.20]. Therefore, it is suggested that $\sqrt{T}$ dependence of the coercivity is favorite in thicker films depending on the nature of the energy barriers.

IV.4 Conclusions

In conclusion, DC current effects on magnetization reversal properties of submicron-sized Py patterns have been investigated. FMR spectroscopy is used to measure the magnetic dynamic process. It is shown that DC current can be used to assist the magnetization reversal. For both 240 nm and 550 nm wide Py patterns the coercivity are reduced by 33%. The magnetization reversal mode will be further investigated in the final dissertation.

Reference

[4.1] P. Wang, H. Zhang, R. Divan and A. Hoffmann, "Tailoring High-Frequency Properties of Permalloy Films via Submicron Patterning," *IEEE Trans. Magn.* **45**, 71 (2009).

[4.2] J. Shi, S. Tehrani, T. Zhu, Y. F. Zheng, and J. –G. Zhu, "Magnetization Vortices and Anomalous Switching in Patterned NiFeCo Submicron Arrays," *Appl. Phys. Lett.* **74**, 2525 (1999).

[4.3] T. Korn, M. Kerekes, U. Ebels, D. Stanescu, and P. Xavier, "Pumping-Field-Induced Dynamic Effects in Micron-Sized Permalloy Lines and Their Influence on HF Filter Applications," *IEEE Trans. Magn.* **41**, 3514 (2005).

[4.4] M. Zhang, Y. Nozaki, and K. Matsuyama, "Reconfigurable Ferromagnetic Resonance Properties in Nanostructured Multilayers," *J. Appl. Phys.* **99**, 08G307 (2006).

[4.5] C. Nistor, K. Sun, Z. Wang, M. Wu, C. Mathieu and M. Hadley, "Observation of Microwave-Assisted Magnetization Reversal in $Fe_{65}Co_{35}$ Thin Films through Ferromagnetic Resonance Measurements," *Appl. Phys. Lett.* **95**, 012504 (2009).

[4.6] H. T. Nembach, H. Bauer, J.M. Shew, M. L. Schneider, and T. J. Silva, "Microwave Assisted Magnetization Reversal in Single Domain Nanoelements," *Appl. Phys. Lett.* **95**, 062506 (2009).

[4.7] D. Atkinson and R. P. Cowburn, "Heat-Assisted Magnetization Switching in Elongated Submicrometer Permalloy Structures," *Appl. Phys. Lett.* **92**, 1386 (2004).

[4.8] R. H. Koch, G. Grinstein, G. A. Keefe, Y. Lu, P. L. Trouiloud, W. J. Gallagher and S. S. P. Parkin, "Thermally Assisted Magnetization Reversal in Submicron-Sized Magnetic Thin Film," *Phys. Rev. Lett.* **84**, 5419 (2000).

[4.9] I. L. Prejbeanu, W. Kula, K. Ounadjela, R. C. Sousa, O. Redon, B. Dieny and J. P. Nozieres, "Thermally Assisted Switching in Exchange-Biased Storage Layer Magnetic Tunnel Junctions," *IEEE Trans. Magn.* **40**, 2625 (2004).

[4.10] C. Papusoi, R. C. Sousa, B. Dieny, I. L. Prejbeanu, Y. Conraux, K. Mackay and J. P. Nozieres, "Reversing Exchange Bias in Thermally Assisted Magnetic Random Access Memory Cell by Electric Current Heating Pulses," *J. Appl. Phys.* **104**, 013915 (2008).

[4.11] C. Papusoi, Y. Conraux, I. L. Prejbeanu, R. Sousa, and B. Dieny, "Switching Field Dependence on Heating Pulse Duration in Thermally Assisted Magnetic Random Access Memories," *J. Magn. Magn. Mater.* **321**, 2467 (2009).

[4.12] J. Herault, R. C. Sousa, C. Ducruet, B. Dieny, Y. Conraux, C. Portemont, K. Mackay, I. L. Prejbeanu, B. Delaet, M. C. Cyrille and O. Redon, "Nanosecond Magnetic

Switching of Ferromagnet-antiferromagnet Bilayers in Thermally Assisted Magnetic Random Access Memory," *J. Appl. Phys.* **106**, 014505 (2009).

[4.13] B. Purnama, T. Tanaka, Y. Nozaki and K. Matsuyama, "Material Dependence of Thermally Assisted Magnetization Reversal Properties in Microstructured Co/Pd Multilayers," *Appl. Phys. Express.* **2**, 033001 (2009).

[4.14] Y.Nozaki, K. Tateishi, S. Taharazako, M. Ohta, S. Yoshimura and K. Matsuyama, "Microwave-Assisted Magnetization Reversal in 0.36-μm-wide Permalloy Wires," *Appl. Phys. Lett.* **91**, 122505 (2007).

[4.15] Y.Nozaki, N. Narita, T. Tanaka and K. Matsuyama, "Microwave-Assisted Magnetization Reversal in A Co/Pd Multilayer with Perpendicular Magnetic Anisotropy," *Appl. Phys. Lett.* **95**, 082505 (2009).

[4.16] Y.Nozaki, K. Tateishi and K. Matsuyama, "Experiments on Microwave-Assisted Magnetization Reversal in a Submicron-Scale Permalloy Single Element with a Zero-Field Resonance Frequency of 6.3 GHz," *Appl. Phys. Express.* **2**, 033002 (2009).

[4.17] W. C. Uhlig and J. Shi, "Systematic Study of the Magnetization Reversal in Patterned Co and NiFe Nanolines," *Appl. Phys. Lett.* **84**, 759 (2004).

[4.18] J. Li, J. Shi and S. Tehrani, "Temperature Dependent Switching Properties of Patterned 200 nm $Ni_{81}Fe_{19}$ Elements," *Appl. Phys. Lett.* **79**, 3821 (2001).

[4.19] S. Goolaup, A. O. Adeyeye, "Magnetization Switching in Alternating Width Nanowire Arrays," *Phys. Rev. B* **75**, 144430 (2007).

[4.20] S. Goolaup, N. Singh, A. O. Adeyeye, V. Ng and M. B. A. Jalil, "Transition from Coherent Rotation to Curling Mode Reversal Process in Ferromagnetic Nanowires," *Eur. Phys. J. B* **44**, 259 (2005).

[4.21] H. Zhang, A. Hoffmann, R. Divan and P. Wang, "Direct Current Effects on High-frequency Properties of Patterned Thin Films," *IEEE Trans. Magn.* **45**, 5296 (2009).

[4.22] Y. Song, C. Romero and M. Wu, "Millimeter Wave Notch Filters Based on Ferromagnetic Resonance in Hexagonal Barium Ferrites," *Appl. Phys. Lett.* **95**, 142506 (2009).

[4.23] B. Kuanr, R. Marson, S. R. Mishra, A. V. Juanr, R. E. Camley and Z. J. Celinski, "Gigahertz Frequency Tunable Noise Suppressor Using Nickel Nanorod Arrays and Permalloy Films," *J. Appl. Phys.* **105**, 07A520 (2009).

[4.24] J. F. Smyth, S. Schultz, D. R. Fredkin, D. P. Kern, S. A. Rishton, H. Schmid, M. Cali, and T. R. Koehler, "Hysteresis in Lithographic Arrays of Permalloy Particles: Experiment and Theory (invited)," *J. Appl. Phys.* **69**, 5262 (1991).

[4.25] IUPAC Goldbook definition.

CHAPTER FIVE

BROADBAND MAG-NOISE OF PATTERNED PERMALLOY THIN FILMS

A Y-factor noise figure (NF) measurement method is developed to characterize high-frequency mag-noise of a 550 nm wide Permalloy strip array under different DC bias currents. The noise voltage density is obtained. Measurement data show that rapid FMR shift induced by DC bias current is related to the excess magnetization fluctuation thermally created by the combined DC current Joule heating effects and orthogonal Oersted fields.

V.1 Introduction

Thermal magnetization noise (mag-noise) has drawn significant attention in the development of magnetoresistive sensors (including recording read heads) and the investigation dynamic properties of nano-scale magnetic structures. The mag-noise presents a fundamental limit on achievable sensor sensitivities (i.e. sensor noise floor), restricts sensor size miniaturization (since mag-noise scales inversely with device volume) and operating frequency extensions [5.1-5.12]. On the other hand, the increased mag-noise provides a powerful approach to characterize the dynamic properties of small magnetic structures, such as dynamic modes and damping processes [5.13-5.15].

So far, the studies of mag-noise were mostly related to spin valve devices (with current flowing in the film plane) and magnetic tunnel junction heads (with current perpendicular to the plane) [5.14]. It is identified that the deviation of (ferromagnetic)

free layer spins from their local equilibrium in these devices is the main physical origin of mag-noise therein [5.13].

Mag-noise also poses a fundamental limit on the application of patterned ferromagnetic thin films in radio-frequency (RF) integrated passive devices, such as inductors, filters and circulators, which are the bottleneck of the dominating complementary-metal-oxide-semiconductor (CMOS) technologies [5.16-5.18]. Patterning is usually used to boost ferromagnetic resonance frequencies (FMR), hence operating frequencies [5.19]. In these devices, DC and RF currents pass through interconnect metal films instead of ferromagnetic thin films. Corresponding dynamic processes are field and thermal driven with intriguing properties [5.20]. Therefore, it is of great interest and practical importance to investigate the associated mag-noise and understand the dynamic processes. Additionally, the obtained results complement the studies on current-driven mag-noise discussed above.

In this work, we study field-driven mag-noise of patterned Permalloy (Py) thin-films with a Y-factor mag-noise measurement method, which measures the noise figure (NF, the ratio of signal to noise ratio at the input port to signal to noise ratio at the output port). Such a two-port method has not been used for mag-noise studies so far. The method is able to directly account for parasitic effects inherent in mag-noise test fixtures and takes advantages of various advanced techniques developed for CMOS transistor and communication circuit characterizations.

V.2 Experiment Arrangements

The test sample (device-under-test, DUT) fabrication process is discussed in previous chapters and our earlier publication [5.21]. Figure V.1 shows the mag-noise measurement system set-up and a scanning electron microscope (SEM) picture of a section of Au line with Py patterns. Contact to the DUT was made via microwave probes. DC bias current is applied to the DUT through two broadband, low insertion loss bias-tees. During measurements, the DC bias is increased from 0 mA to 50 mA. The output is amplified by a commercial broadband (0.01-18 GHz) 33 dB gain low noise amplifier (LNA, 2.5 dB NF, B&Z BZP114UB). Finally the amplified noise output is captured by a spectrum analyzer (Rhode & Schwarz FSE), with a bandwidth resolution set to 1 MHz to measure the noise figure from 2 GHz to 10 GHz. System calibrations were performed before connecting the DUT so that all subsequent measurements can use corrections and the corrected NF can be obtained. Both NF and system power gain, G_S, can be measured and recorded simultaneously with the FS-K3 software of the spectrum analyzer. The CPW resistances at different bias currents are also measured concurrently to extract temperature changes of the on-chip transmission line.

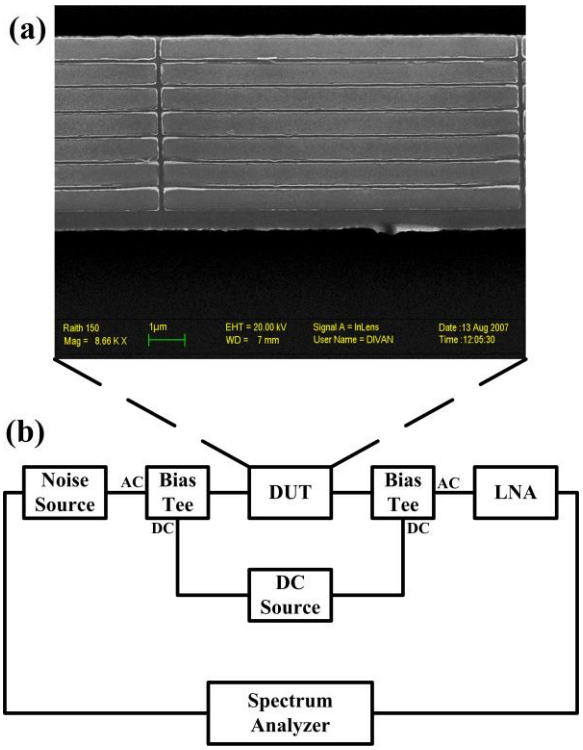

Figure V.1 (a) SEM picture of a ~ 550 nm Py array under test and (b) Y-parameter mag-noise measurement system setup.

V.3 Results and Discussions

Figure V.2 (a) shows the measured broadband NF with the patterned Py DUT under several DC bias currents, I_{DC}. The measured NF increases as a function of frequency because of the increased loss of the components in the system. The multiple resonances in the spectrum may come from the mismatch between the DUT, bias tee and LNA [5.10]. The NF increases monotonically with bias currents except that the curves intercept around 8 GHz. The reason for this will be discussed momentarily. The noise voltage density (NVD, V_N) can be extracted from the equation as in [5.22]

$$F = \frac{N_a + kT_0G_S}{kT_0G_S} \tag{V.1}$$

where F is the noise figure in linear terms, N_a is the added noise of the whole system, k is the Boltzmann's constant, G_S is the system power gain and $T_0 = 290\,K$ is the reference temperature. The mag-noise of the patterned Py array can be evaluated from the measured NVDs by subtracting NVDs of an identical transmission line without Py array loaded. Figure V.2 (b) shows the extracted NVD of the Py array for various bias currents. A pronounced FMR like peak appears for different biases. As the bias current increases, the resonance peak power increases while the resonance frequency decreases. For 40 mA and 50 mA DC current cases, the significantly increased tail at frequencies higher than FMR frequencies is likely due to significant nonuniformity of Py pattern magnetization caused by the Joule heating effects [5.10], [5.20]. A comparison between the transmission coefficients measured with an HP 8510C vector network analyzer and the NVDs at 10 mA and 50 mA is shown in Figure V.3. The corresponding resonance peaks at different bias currents for both measurements are about the same. The close correlation between the NVD peaks and the FMR peaks of the transmission coefficients shows that the excess noise is magnetic in origin. The NVD peaks around 8 GHz account for the convergence of the NF shown in Figure V.2 (a). The peak shift cannot be easily observed from Figure V.2 (a) because the noise figures are measurement results for the whole system (bias tees, LNA, and transmission line) and the information of the Py array is somehow overwhelmed. The information of the Py array is clear after the de-embedding process (by subtracting the reference line data) as shown in Figure V.2 (b).

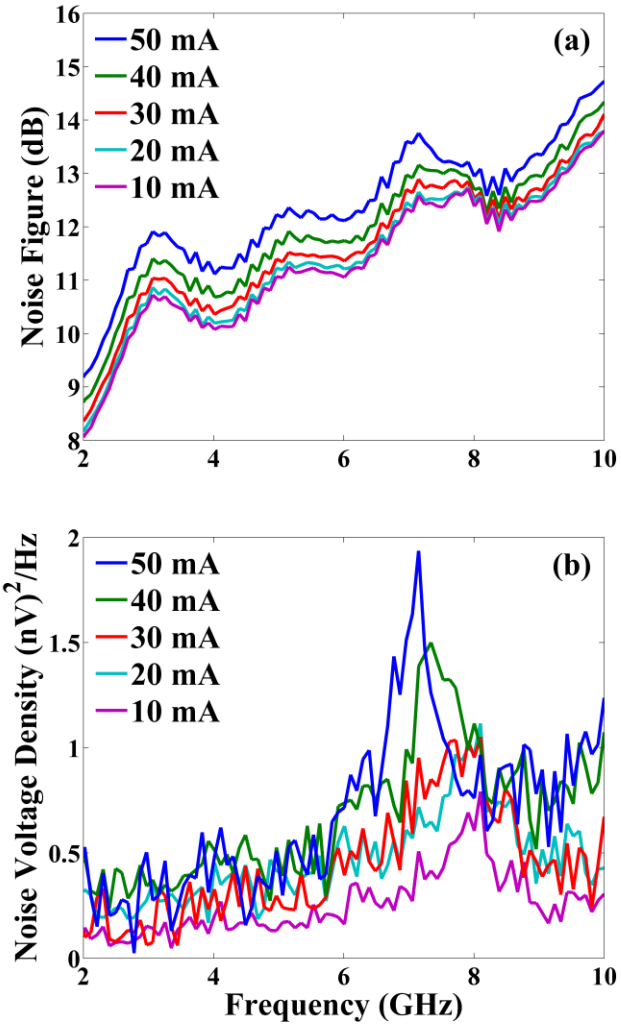

Figure V.2 (a) Measured noise figure of a 550 nm Py array loaded transmission line. (b) Extracted noise voltage density of the 550 nm Py array.

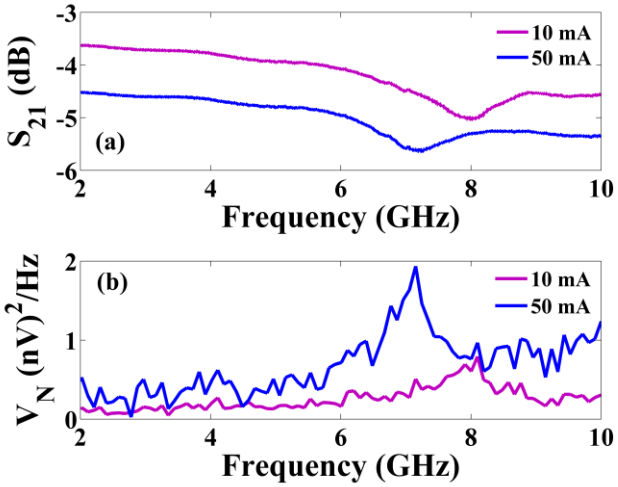

Figure V.3 Comparison between the measured transmission coefficients and the noise voltage density of the 550 nm Py array under 10 and 50 mA DC currents. The top figure shows the transmission coefficients. The bottom figure shows the measured noise voltage density.

Fluctuation-dissipation theorem was commonly used for mag-noise characterizations in spin valve devices, in which DC current passes through the stacked multilayer structure and the noise spectra has a relationship with the magnetoresistance change [5.1], [5.15]. In our samples, both the DC and RF current pass through the transmission line bearing the Py array and exert magnetic field in the hard axis direction of the Py array. A lumped RLCG (resistance, inductance, capacitance and conductance) transmission line model, shown in Fig. 4 (a), can be used to describe the broadband electrical properties of Py arrays with ΔR characterizing Py mag-noise properties in such a configuration. Here, R and L are the resistance and inductance of the Au transmission line; ΔR and ΔL are the resistance and inductance perturbation from the Py array; C and

G are the capacitance and conductance of the quartz substrate. The influence of the capacitance of the Py array is negligible because the Py pattern is sputtered on top of the transmission line with a relatively thin ~100 nm thickness.

The measured noise is considered to be Johnson-Nyquist noise from the real part of the high frequency impedance of the Py array in this magnetic field driven situation. The equivalent noise power transfer circuit is shown in Fig. 4 (b). The NVD V_N from the Py array is written as

$$V_N = 4NkT\Delta R \tag{V.2}$$

where N is the total Py element number in the array, $\Delta R + R$ is read from the DC current source.

The frequency dependent high frequency impedance of an amorphous ferromagnetic thin film can be calculated by solving the Maxwell equations and the linearized Landau-Lifshitz equation simultaneously, and is written as in [5.24]

$$Z = R_{DC}\frac{\eta a}{2}\coth\left(\frac{\eta a}{2}\right) \tag{V.3}$$

$$\eta = \sqrt{i\omega\mu_{eff}\sigma}$$

where R_{DC} is the direct current resistance of a Py element, a is the thickness of the film and σ is the conductivity of the film. The effective permeability of the Py pattern can be written as in [5.25]

$$\mu_{eff} = \frac{4\pi M_s\gamma^2\left(j\omega\alpha/\gamma + 4\pi M_s N_z\right)}{\omega^2 - j\left(2H_k + 4\pi M_s\left(1-N_x\right)\right)\omega\alpha\gamma - \omega_f^2} + 1 \tag{V.3}$$

where $4\pi M_s = 9\ kG$ is the saturation magnetizations, $\gamma = 176\ GHz/T$ is the gyromagnetic ratio, α is the damping constant, ω_f is the measured FMR angle frequency, H_k is the magnetocrystalline anisotropy field, N_x and N_z are the demagnetization factors in the sample length and thickness directions. Since the fabricated Py structures are rectangular prisms, their demagnetization factors can be calculated by using the equations in [5.26]. A value of $\alpha = 0.02$ is used in our calculation according to [5.27]. The resistance change of the transmission line associated with the Joule heating effects from the applied DC currents has been taken into account. The measured and calculated NVDs of the sample under DC currents of 10, 40 and 50 mA are compared in Fig. 5. The symbols are measurement data and the solid lines are theory values. They agree with each other well. Both measurement and theory results show that the noise power increases with respect to the applied DC current. The increased thermal fluctuation could be responsible for our previous observation that the FMR shift is much faster with a ~50 mA DC current passing through the transmission line than that is in an external static magnetic field of the same magnitude.

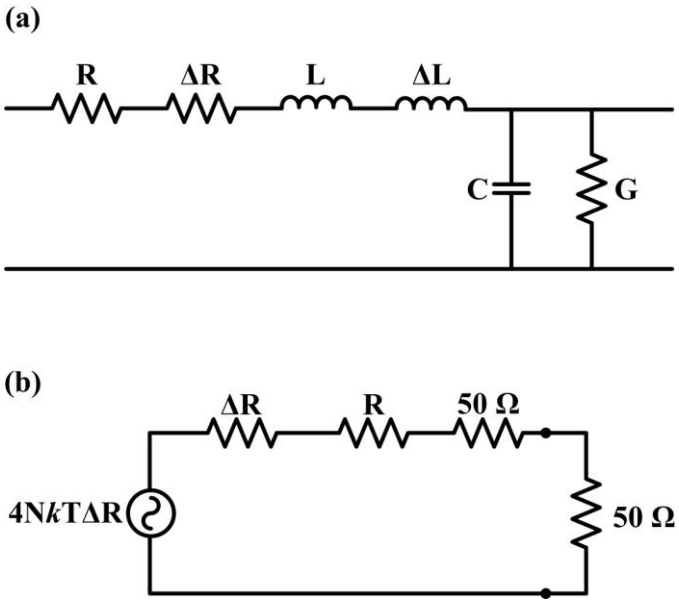

Figure V.4 (a) Lumped RLCG model for the Py array loaded transmission line and (b) equivalent noise power transfer circuit. The noise source counts for the Py array, the other resistance in the circuit are noiseless because the de-embedding procedures were performed during measurements.

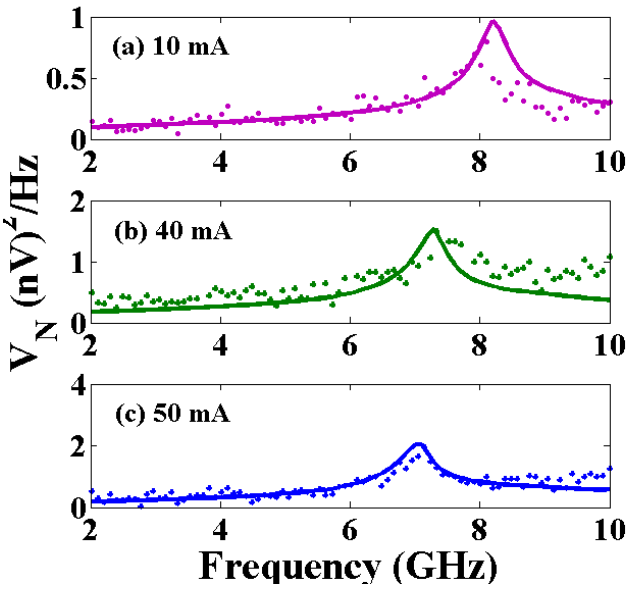

Figure V.5 Comparison between the measurement data and the calculated data of NVDs under different DC currents. The symbols are the measurement data and the solid lines are the calculated data. (a) 10 mA DC current, (b) 40 mA DC current, and (c) 50 mA DC current.

V.4 Conclusions

We demonstrated that noise figure measurement method can be used to characterize high-frequency mag-noise of sub-micronsize ferromagnetic Py array. Parasitic effects can be de-embedded. Measurement data show that rapid FMR shift induced by DC bias current is related to the excess magnetization fluctuation thermally created by the combined DC current effects of Joule heating and orthogonal Oersted fields. The proposed lumped transmission line circuit model describes mag-noise properties of the patterned Py array characteristics well. Measurement data show that rapid FMR shift induced by DC bias current is related to the excess magnetization fluctuation thermally created by the combined DC current effects of Joule heating and orthogonal Oersted fields.

Reference

[5.1] N. Smith and P. Arnett, "White-Noise Magnetization Fluctuations in Magnetoresistive Heads**,**" *Appl. Phys. Lett.* **78**, 1448 (2001).

[5.2] N. Smith and P. Arnett, "Thermal Magnetization Noise in Spin Valves," *IEEE Trans. Magn.* **38**, 32 (2002).

[5.3] M. Pannetier, C. Fermon, G. Goff, J. Simola, E. Kerr, "Femtotesla Magnetic Field Measurement with Magnetoresistive Sensors**,**" *Science.* **304** 1648 (2004).

[5.4] Neil Smith, "Modeling of Thermal Magnetization Fluctuations in Thin-Film Magnetic Devices," *J. Appl. Phys*. **90**, 5768 (2001).

[5] Neil Smith, V. Synogatch, D. Mauri, J. A. Katine, and Marie-Claire Cyrille, "Thermal Magnetization Fluctuations in CoFe Spin-valve Devices," *J. Appl. Phys.* **91**, 7454 (2002).

[5.6] V. L. Safonov and H. N. Bertram, "Thermal Magnetization Noise in a Thin Film," *Phys. Rev. B.* **65**, 172417 (2002).

[5.7] Jian-Gang Zhu, "Thermal Magnetic Noise and Spectra in Spin Valve Heads," *J. Appl. Phys*. **91**, 7273 (2002).

[5.8] O. Heinonen and H. S. Cho, "Thermal Magnetic Noise in Tunneling Readers," *IEEE Trans. Magn*. **40**, 2227 (2004).

[5.9] Y. Zhou, "Thermally Excited Magnetic Noise from Pinned and Reference Layers in Current Perpendicular-to-plane Structure Magnetoresistive Heads," *J. Appl. Phys*. **103**, 07F516 (2008).

[5.10] J.C. Jury, K. B. Klaassen, J. C. L. Peppen and S. X. Wang, "Measurement and Analysis of Noise Sources in Giant Magnetoriesistive Sensors Up to 6 GHz," *IEEE Trans. Magn*. **38**, 3545 (2004).

[5.11] Z. Jin and H. N. Bertram, "Experimental Measurements and Analysis of Thermal Magnetization Noise in GMR Sensors," *IEEE Trans. Magn*. **38**, 2265 (2002).

[5.12] S. H. Liou, R. Zhang, S. E. Russek, L. Yuan, S. T. Halloran and D. P. Pappas, "Dependence of Noise in Magnetic Tunnel Junction Sensors on Annealing Field and Temperature," *J. Appl. Phys*. **103**, 07E920 (2008).

[5.13] N. A. Stutzke, S. L. Burkett and S. E. Russek, "High-frequency Noise Measurements in Spin-valve Devices," *J. Vac. Sci. Technol.* **A 21**, 1167 (2003).

[5.14] V. Synogatch and N. Smith and J. R. Childress, "Ferromagnetic Resonance in Tunnel Junctions: Mag-noise and Complex Impedance Analysis," *J. Appl. Phys.* **93**, 8570 (2003).

[5.15] N. Stutzke, S. L. Burkett and S. E. Russek, "Temperature and field dependence of high-frequency magnetic noise in spin valve devices," *Appl. Phys. Lett.* **82**, 91 (2003).

[5.16] J. Salvia, J. A. Bian and C. P. Yue, "Tunable On-chip Dinductors up to 5 GHz using Patterned Permalloy Laminations," *IEDM Tech. Dig.* 943 (2005).

[5.17] B. Kuanr, V. Veerakumar, R. Marson, S. Mishra, R. E. Camley and Z. Celinski, "Nonreciprocal Microwave devices Based on Magnetic Nanowires," *Appl. Phys. Lett.* **94**, 202505 (2009).

[5.18] J. W. Wang, S.D. Yoon, V.G. Harris, C. Vittoria, and N.X. Sun, "Integrated Metal Magnetic Film Coupled Line Circulators for Monolithic Microwave Integrated Circuits," *Electron. Lett.* **43**, 292 (2007).

[5.19] X. Chen, Y. G. Ma and C. K. Ong, "Magnetic Anisotropy and Resonance Frequency of Patterned Soft Magnetic Strips," *J. Appl. Phys.* **104**, 013921 (2008).

[5.20] H. Zhang, A. Hoffmann, R. Divan, P. Wang, "Direct Current Effects on High-frequency Properties of Patterned Permalloy Thin Films," *IEEE Trans. Magn*. **45**, 5296, (2009).

[5.21] P. Wang, H. Zhang, R. Divan and A. Hoffmann, "Tailoring High-frequency Properties of Permalloy Films by Submicrometer Patterning," *IEEE Trans. Magn*. **45**, pp. 71 (2009).

[5.22] Fundamental of RF and Microwave Noise Figure Measurements, Hewlett-Packard Application. Note 57-1, Santa Rosa, CA 1983.

CHAPTER SIX

LOW FREQUENCY NOISE OF PATTERNED THIN FILMS

Detailed investigations of 1/*f* noise were performed in Permalloy microwires. The gold bridges for the four probe measurement setup were deposited on a quartz substrate. Pattern geometry and bias current effects on the material's 1/*f* noise were studied. The normalized Hooge parameter and frequency slope were analyzed in the framework of the empirical Hooge relation. The quadratic dependence of the noise power spectral density versus bias current was verified. However, both the normalized Hooge parameter and frequency slope were pattern width dependent. We attribute this to the pattern geometry related magnetic state and magnetic domain wall configuration differences in the magnetic films.

VI.1 Introduction

Magnetic thin film magnetoresistive (MR) sensors are widely used in magnetic storage industry. They are also promising candidates for detecting magnetically labeled biomarkers and scanning MR microscopy. Such applications require subnanotesla or even femtotesla sensitivity at low frequencies [6.1-6.2]. Patterned magnetic thin films have also attracted much attention in the development of high-performance complementary metal-oxide-semiconductor (CMOS) integrated circuit (IC) components, such as inductors, high-speed interconnects and nonreciprocal spin wave devices [6.3-6.5]. Sensor sensitivity and IC component performance are ultimately limited by the

intrinsic noise and extrinsic factors such as biasing direct current (DC) in ICs and sensing current in hard disk heads, both of which have attracted intense interest [6.6-6.8].

The $1/f$ noise is usually described by Hooge empirical formula as following [6.9]:

$$\frac{S_V}{V^2} = \frac{\alpha_H}{n} \times \frac{1}{\Omega \times f^{\gamma}}$$

where S_V is the noise power spectral density, V the sample voltage, α_H the Hooge parameter, n the charge carrier density, Ω the sample volume, f the frequency, γ the frequency slope.

DC current effects on $1/f$ noise in MR devices and patterned colossal magnetoresistive manganite thin films have been studied previously [6.10-6.11]. In these studies DC current passes through magnetic films. However, in CMOS IC applications, DC current mainly passes through the nonmagnetic layer of circuit components such as the copper layer of the inductors and interconnections rather than the magnetic thin films. Unique DC effects on magnetization dynamics such as broadband mag-noise and magnetization reversal of such magnetic thin films have been observed in these situations [6.8], [6.12]. Nevertheless, there is little information regarding $1/f$ noise of patterned ferromagnetic thin films for CMOS ICs. In this chapter we report our results on DC current effects on $1/f$ noise in Permalloy (Py=$Ni_{80}Fe_{20}$) microwires for the first time. They are measured with a four probe scheme. The dependences of $1/f$ noise on pattern geometry and DC currents are studied.

VI.2 Experiment Methods

A group of 500 nm thick gold bridges with width and length ($W \times L$) of 10×180 μm^2 and four contact pads were fabricated on top of a quartz substrate. Two pads are for supplying the current (I^+, I^-) and two for carrying out the voltage measurements (V^+, V^-). The one step production of the bridge and contact pads is designed for low resistive four-probe connections. After the gold layer deposition, a stack of Cr (8 nm)/Py (100 nm) thin films were deposited by e-beam evaporation on top of the bridges. They were patterned to different lateral dimensions with widths and length ($W \times L$) of 2×100 μm^2, 5×100 μm^2, and 10×100 μm^2 by lift-off. Each pattern is positioned at the center of the gold bridges. One bridge with a 10 μm wide Py pattern is shown in Figure VI. 1. The connection between the external circuitry and the bridge contact pads were made with GGB DC probes.

As shown in Fig. 1, the bias current is supplied from a Keithley 2612 current source passing through the gold bridge. Oersted field and Joule heating effects of the DC current on the $1/f$ noise are investigated with this setup. The noise signal was picked up from the voltage probes with a vector signal analyzer Agilent 89441A. The resolution bandwidth (RBW) was set to be 1Hz, and 3000 measurements were made for each sweep in the frequency range of 1 Hz to 100 Hz. The average value of the noise voltage was recorded. The noise floor of the measurement system was about 2.6e-11 V^2/Hz at 1Hz. No external amplifier was used in all the measurements.

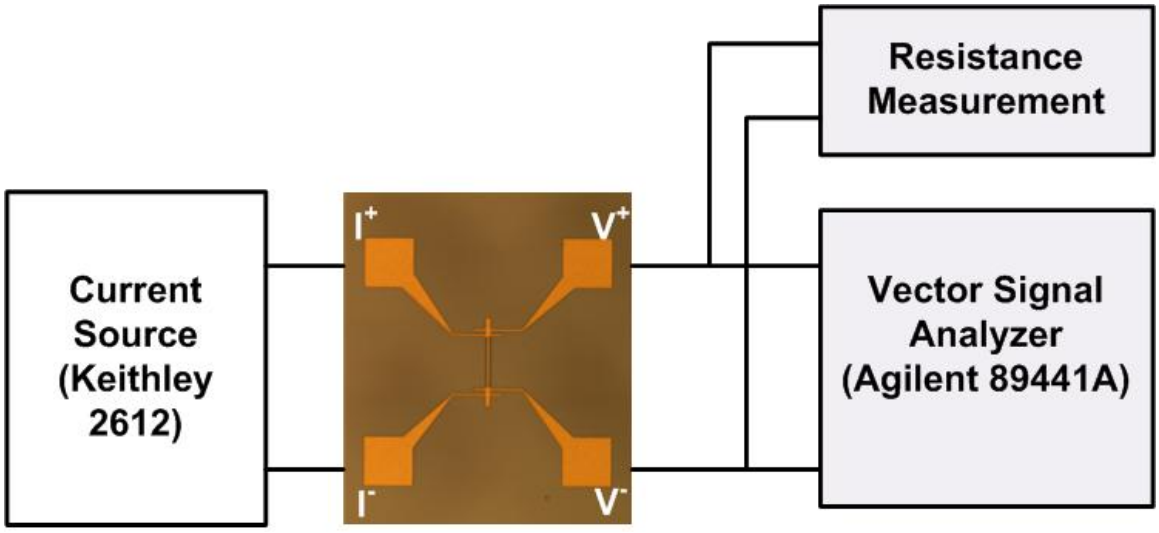

Figure VI.1 Schematic of the measurement setup.

VI.3 Results and Discussions

Figure VI. 2 shows the typical noise power spectral density curve as a function of frequency for different bias currents. The measurements were carried out in a 100 nm thick, 2 μm wide and 100 μm long Py pattern at room temperature. The slopes of the low frequency noise vary from 0.8 to 1.3 versus bias current in the 1-100 Hz range. The dependence of 1/*f* noise on the bias current is also investigated. Figure VI. 3 (a), (b), (c) and (d) show the noise power spectral density at 1 Hz as a function of the square of the biasing current for 2 μm, 5 μm, 10 μm wide Py patterns and a reference line without Py, respectively. The results show that the noise power spectral density of the transmission line without magnetic material is almost linear with the square of the bias current. However, the noise power spectral densities of the transmission lines with magnetic materials are not linearly dependant, which conflicts with Hooge formula and indicates that the noise was not due to resistance fluctuations in the magnetic materials and the transmission lines.

The normalized Hooge parameter α_H / n and frequency slopes γ are deduced as a function of bias current and pattern width. The results show that the normalized Hooge parameter decreases with increasing bias current in the entire current range for the 10 μm wide pattern. For 2 μm and 5 μm wide patterns the normalized Hooge parameter decreases when the bias current is lower than 80 mA and has a rising tail when the current is increased to 100 mA. The pattern width dependence of the normalized Hooge parameter is also clearly observed in Figure VI. 4. In each film, the wider the pattern the higher the normalized Hooge parameter, except for the 100 mA bias current. This width

dependence of the normalized Hooge parameter has also been reported in the previous literature [6.11]. Since α_H / n is an intrinsic parameter of the material, we attribute its current and pattern width dependence to the domain structure reconfiguration and domain wall fluctuation. It should be noted that the mechanism of the DC current effects on such large dimensional Py patterns is different from that in nanoscale Py patterns reported before, where the Joule heating effects play a major role [6.5]. The Joule heating effect is minor here because the temperature variation is small which can be calculated from the device resistance change. At each bias current, the resistance of the device under test in was measured simultaneously and only a less than 5% increase was observed. Compared with the nanoscale patterns in which uniform magnetization distribution is dominant, more complicated Landau and diamond domain structures are expected in the films studied here [6.12]. The other important effect, the Oersted field of the DC current is estimated with Ampere's law $H_{DC} = I/2w$, where I is the DC and w is the width of the transmission line [6.15]. When the current is increased to 80 mA, the calculated Oersted field is 4 KA/m, which could assist the alignment of magnetic domain walls and reduce the fluctuations. As a result the normalized Hooge parameter decreases as the Oersted field becomes stronger. When the current keeps increasing the Joule heating effects will compete with the Oersted field effects to promote the fluctuations and the final results become unpredictable.

The frequency slopes are shown in Figure VI. 5. The frequency slopes do not vary with the bias currents for narrower patterns, except for 100 mA current. The frequency slopes for 5 μm and 10 μm patterns are close to each other in the bias current range. The

2 μm pattern has a 50% higher frequency slope value. This width dependence of frequency slope is unexpected, and it has not been reported in the literature. Nevertheless, additional experiments are needed to investigate the magnetic state and structural origin of the observation.

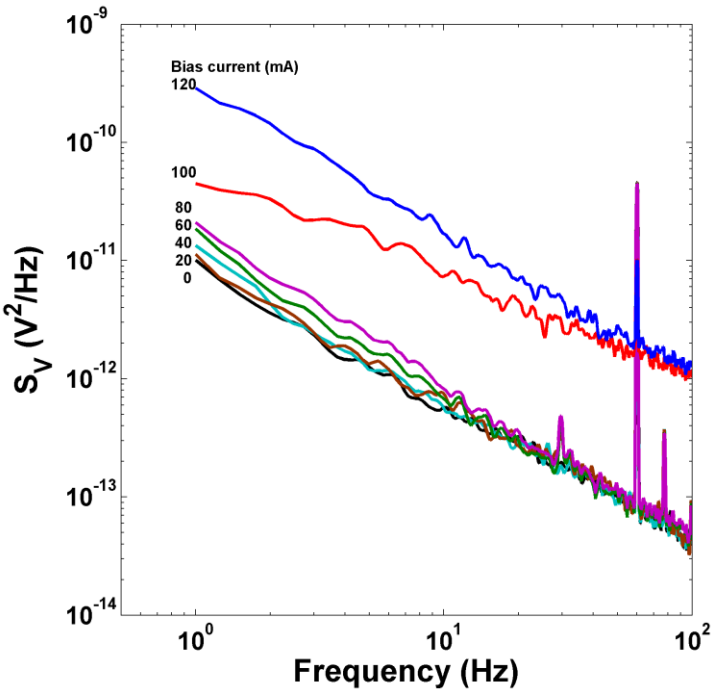

Figure VI.2 The measured low frequency noise versus frequency and bias current in a 100 nm thick, 2 µm wide and 100 µm long Py pattern.

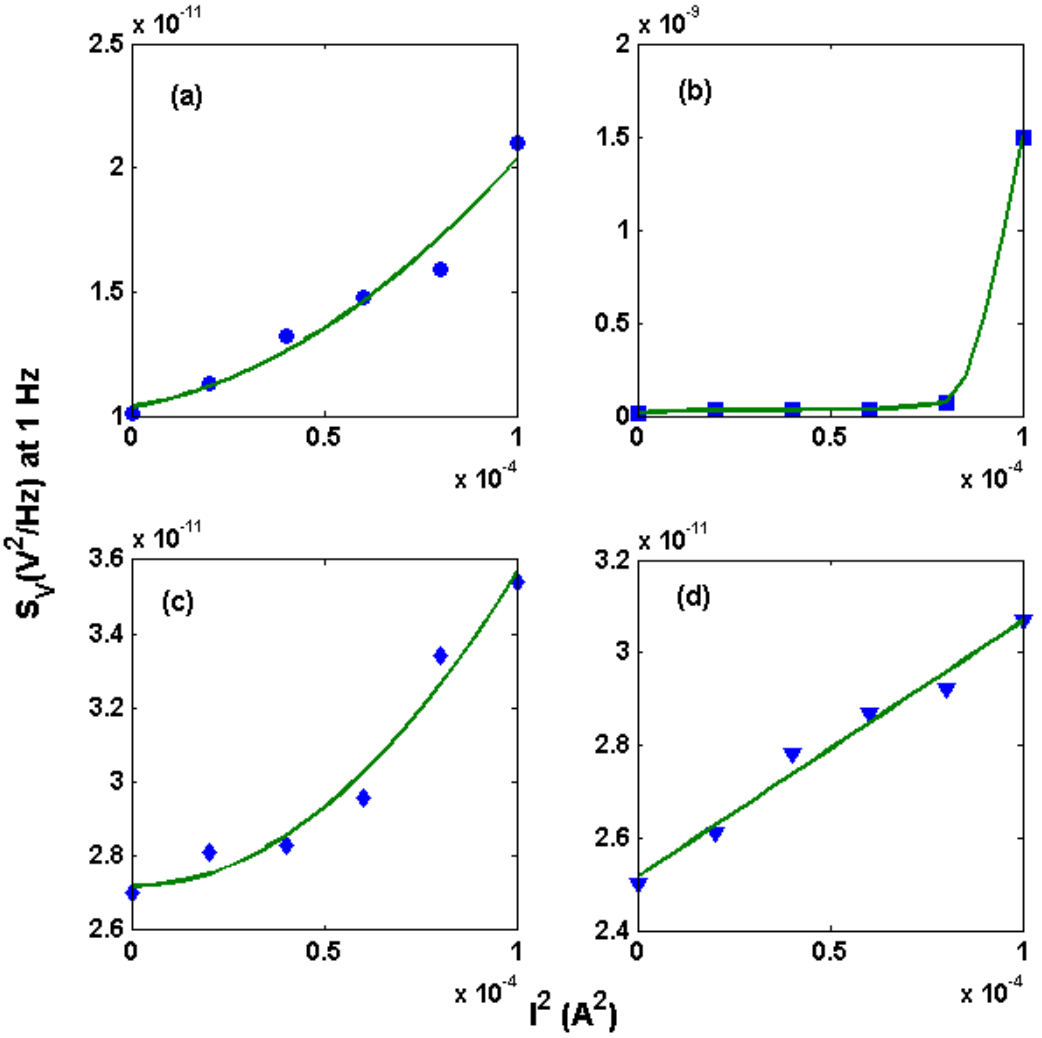

Figure VI.3 Noise power spectral density at 1 Hz as a function of the square of the biasing current for (a) 2 μm, (b) 5 μm, (c) 10 μm wide Py patterns and (d) a reference line without Py.

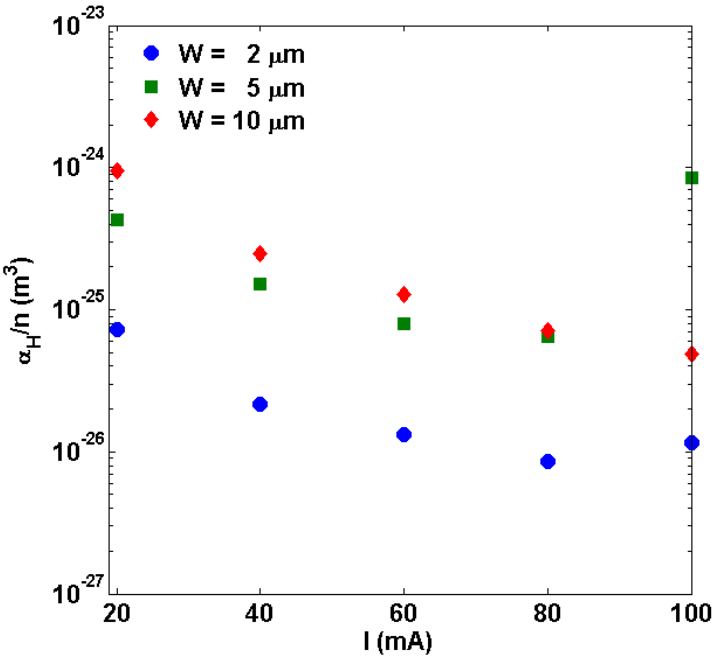

Figure VI.4 Deduced normalized Hooge parameters versus bias current and pattern width.

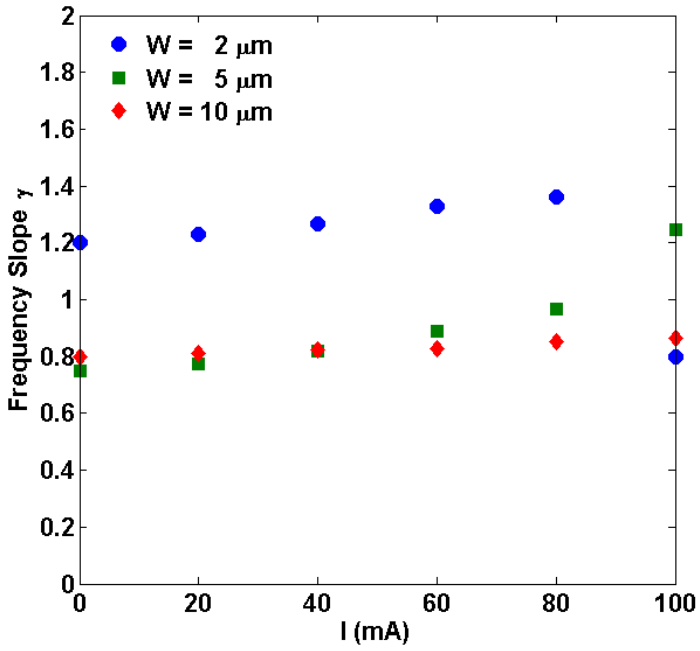

Figure VI.5 Deduced frequency slopes versus bias current and pattern width.

VI.4 Conclusion

We have measured the 1/*f* noise in patterned Py microstructures in a configuration that the bias current does not pass through the magnetic material directly. The normalized Hooge parameter and frequency slope were found pattern width dependent unexpectedly. This suggests that the magnetization state in the films affects the 1/*f* noise significantly. The 1/*f* noise measurement in this configuration is for the first time carried out. It provides more information for better use of such ferromagnetic materials in CMOS ICs. The results are complementary to the 1/*f* noise measurement. They are quite helpful for the understanding of low frequency noise and of essential interests in applications such as racetrack memory, magnetic domain wall logic and small magnetic field sensors.

References

[6.1] A. Ozbay, A. Gokce, T. Flanagan, R. A. Stearrett, E. R. Nowak, and C. Nordman, "Low Frequency Magnetoresistive Noise in Spin-Valve Structures," *Appl. Phys. Lett.* **94**, 202506 (2009).

[6.2] M. Pannetier, C. Fermon, G. Goff, J. Simola, and E. Kerr, "Femtotesla Magnetic Field Measurement with Magnetoresistive Sensors," *Science,* **304**, 1648 (2004).

[6.3] D. S. Gardner, G. Schrom, P. Hazucha, F. Paillet, T. Karnik, S. Borkar, R. Hallstein, T. Dambrauskas, C. Hill, C. Linde, W. Worwag, R Baresel, and S Muthukumar, "Integrated On-Chip Inductors Using Magnetic Material (Invited)," *J. Appl. Phys.* **103**, 07E927 (2008).

[6.4] P. Wang, N.C. Tien, E.C. Kan, "Permalloy Loaded Transmission Lines for High-Speed Interconnect Applications," *IEEE Trans. Electron Dev.* **51**, 74 (2004).

[6.5] P. Amiri, B. Rejaei, M. Vroubel, and Y. Zhuang, "Nonreciprocal Spin Wave Spectroscopy of Thin Ni–Fe Stripes," *Appl. Phys. Lett.* **91**, 062502 (2007).

[6.6] H. Zhang, A. Hoffmann, R. Divan and P. Wang, "Direct Current Effects on High-frequency Properties of Patterned Permalloy Thin Films," *IEEE Trans. Magn.* **45**, 5296 (2009).

[6.7] H. Zhang, A. Hoffmann, R. Divan and P. Wang, "Direct-Current Effects on Magnetization Reversal Properties of Submicron-Size Permalloy Patterns for Radio-Frequency Devices," *Appl. Phys. Lett.* **95**, 232503 (2009).

[6.8] M. Xiao, K. B. Klaassen, J. C. L. Peppen, M. H. Kryder, "Extra-Low-Frequency Noise in Giant Magnetoresistance Recording Heads," *J. Appl. Phys.* **85**, 5855 (1999).

[6.9] F. N. Hooge, "1/f Noise Is No Surface Effect," *Phys. Lett.* **29A**, 139 (1969).

[6.10] S. W. Stokes, W. L. Wilson and B. M. Lairson, "Current Density and AC Field Effects on 1/f noise in Spin Valve Sensors," *J. Appl. Phys.* **85**, 4469 (1999).

[6.11] L. Méchin, J. Routoure, S. Mercone, F. Yang, S. Flament, and R. A. Chakalov, "1/f Noise in Patterned $La_{2/3}Sr_{1/3}MnO_3$ Thin Films in The 300–400 K Range," *J. Appl. Phys.* **103**, 083709 (2008).

[6.12] H. Zhang, C. Li, A. Hoffmann, R. Divan and P. Wang, "Broadband Mag-Noise of Patterned Permalloy Thin Films," *IEEE Trans. Magn.* **46**, 2442 (2010).

[6.13] S. Azeemuddin, A. Hoffmann, R. Divan, M. J. Donahue, S. H. Chung and P. Wang, "High-Frequency Domain-Wall Motion and Magnetization Rotation of Patterned

Permalloy Films under External Magnetic Field Excitation," *Nanotechnology,* 6th IEEE Conference on, **2**, 853 (2006).

[6.14] T. J. Silva, C. S. Lee, T. M. Crawford, and C. T. Rogers, "Inductive Measurement of Ultrafast Magnetization Dynamics in Thin-Film Permalloy," *J. Appl. Phys.* **85**, 7849 (1999).

[6.15] A. Yamaguchi and K. Motoi, "Broadband Ferromagnetic Resonance of $Ni_{81}Fe_{19}$ Wires Using a Rectifying Effect," *Phys. Rev. B.* **78**, 104401 (2008).

CHAPTER SEVEN

A NEW METHOD FOR HIGH-FREQUENCY CHARACTERIZATION OF PATTERNED FERROMAGNETIC THIN FILMS

A new microwave measurement method is presented for patterned ferromagnetic thin film characterization. Background noise of the measurement device, which often overwhelms the signal from patterned ferromagnetic structures, is significantly reduced through an on-chip interference process. As a result, the measurement sensitivity is greatly improved compared with conventional transmission line based ferromagnetic resonance (FMR) methods. Algorithms are given to extract the complex permeability and FMR line width of ferromagnetic materials under test. A 10 GHz prototype device was fabricated and a Py array with 180 patterned Py stripes was measured. Each stripe is 100 nm thick, 2 μm wide and 20 μm long. Based on the same design principle, a new device with a more symmetric structure and a field enhancement configuration was proposed and fabricated. The new device has a more than 20 dB sensitivity improvement compared with its prototype. The magnetization dynamics of a 240 nm wide, 5 μm long and 70 nm thick single Py nanowire is investigated with the advanced device. The measurements and full wave three dimensional simulations show that the new method has the capability to study the fundamental physics of nanoscale magnetic devices.

VII.1 Introduction

Ferromagnetic resonance (FMR) is the main technique for the investigation of magnetization dynamics of patterned magnetic structures, which are of great interest for fundamental physics studies and for high speed memory, magnetic storage and signal-processing applications [7.1-7.2]. In the conventional FMR measurement approaches, the FMR signal of a patterned ferromagnetic structure is usually weak compared with the background noise from the measurement devices. As a result, a large number of micro or nanoscale ferromagnetic structures are usually used to enhance FMR signals and de-embedding procedures are exploited to subtract the device parasitic effects. Consequently, variations from one magnetic structure to another are averaged out and FMR distribution begins to affect the results. In addition the accuracy of the subtraction procedures, which deal with parameters that are very close to each other, depends on the reproducibility of the de-embedding structures and of making physical probing. Therefore, it is of great interest to develop new techniques that can enhance FMR measurement sensitivities.

Various new FMR methods have been proposed, including a spin-transfer-driven FMR measurement method which uses spin-transfer torque in a layered magnetic structure for precession excitation [7.3], FMR force microscopy which uses a scannable probe field for FMR modes imaging [7.4], and scanning thermal FMR microscopy which has a spatial resolution in 10 nm range [7.5]. In this chapter, we present an on-chip microwave interferometer, which automatically cancels out the inherent common-mode background signal of the device in a splitting-rejoining-subtraction fashion. Thus the

conventional procedure of subtracting a control signal is eliminated. This idea is a fueling advance in low-noise high-sensitivity magnetic material measurements, biological sensors and polarization-transparent microphotonic devices [7.6-7.9]. Section 2 describes the measurement principle and a prototype device. A Py array consisting of 180 micrometer size Py structures was characterized. Section 3 presents an advanced device with a 20 dB sensitivity improvement compared with its prototype shown in section 2. The FMR and damping properties of a single nanoscale Py wire (70 nm thick, 0.24×5 μm^2 lateral size, inset of Figure VII. 8) were measured at radio-frequencies (rf). The extracted line width and damping constant at 4.3 GHz are 120 Gauss and 0.038, respectively. To our knowledge, this is the smallest ferromagnetic single layer structure that has been characterized through FMR measurement so far.

VII.2 Background Signal Cancellation and FMR Sensitivity Improvement

The proposed FMR measurement structure prototype is shown in Figure VII. 1(a). Unlike the low loss structures discussed in [7.10], on-chip transmission line losses are severe and must be considered for the intended FMR measurement sensitivity improvements.

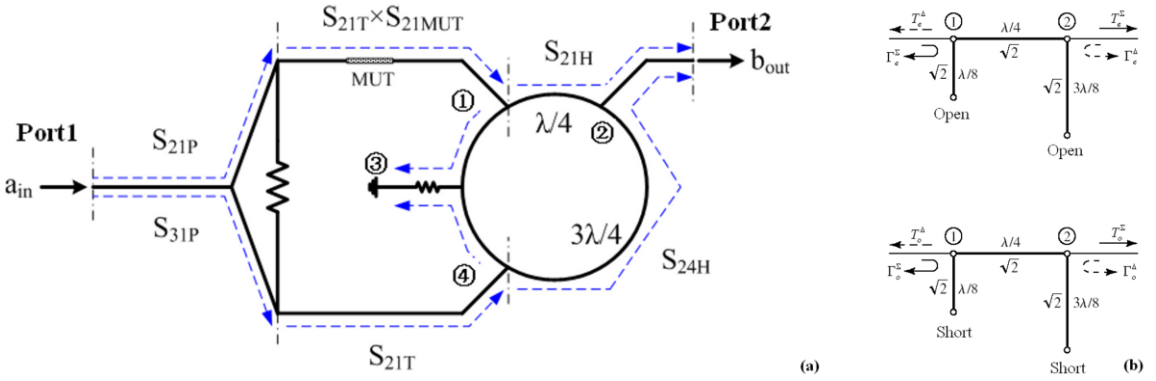

Figure VII.1 (a) Schematic of the measurement structure and the transmission parameter definitions. For simplicity, we assume the same transmission parameter S_{21T} for the top and bottom branches since the length of MUT is negligible. (b) Even and odd mode decomposed networks of the hybrid are shown in the upper and lower panels, respectively.

VII.2.1 Analysis of Proposed FMR Measurement Method

The structure is composed of a Wilkinson power divider and a ring hybrid. The incoming signal from port 1 is split evenly via the power divider into two branches. Signals transmitted through the upper branch, which has the material under test (MUT), and the lower branch add together at port 2. The measured scattering parameter is:

$$S_{21} = b_{out}/a_{in} = S_{21P} \times S_{21T} \times S_{21MUT} \times S_{21H} + S_{31P} \times S_{21T} \times S_{24H} \qquad \text{(VII. 1)}$$

where S_{21P} and S_{31P} are the transmission scattering parameters of the power divider; S_{21T} and S_{21MUT} are the transmission scattering parameters of the straight transmission line and the MUT sections, respectively; S_{21H} and S_{24H} are the transmission parameters of the ring hybrid. When the conductance loss difference of $\lambda/4$ and $3\lambda/4$ sections are

negligible, the interference between the signals from S_{21H} and S_{24H} will significantly reduce the background signals. As a result, the ratio of FMR signal to background signal is dramatically improved, so is the FMR measurement sensitivity.

On-chip transmission lines are usually lossy due to limited line dimensions. So the conductor loss difference in S_{21H} and S_{24H} must be considered. Corresponding expressions of S_{21H} and S_{24H} can be obtained with even-odd mode analysis [7.11].

$$\begin{aligned} S_{21H} &= T_e^{\Sigma}/2 + T_o^{\Sigma}/2,\ T_{e,o}^{\Sigma} = \frac{2}{A_{e,o}^{\Sigma} + B_{e,o}^{\Sigma}/Z_0 + C_{e,o}^{\Sigma} Z_0 + D_{e,o}^{\Sigma}} \\ S_{24H} &= \Gamma_e^{\Delta}/2 - \Gamma_o^{\Delta}/2,\ \Gamma_{e,o}^{\Delta} = \frac{A_{e,o}^{\Delta} + B_{e,o}^{\Delta}/Z_0 - C_{e,o}^{\Delta} Z_0 - D_{e,o}^{\Delta}}{A_{e,o}^{\Delta} + B_{e,o}^{\Delta}/Z_0 + C_{e,o}^{\Delta} Z_0 + D_{e,o}^{\Delta}} \end{aligned} \qquad \text{(VII.2)}$$

$T_{e,o}^{\Sigma}$ and $\Gamma_{e,o}^{\Delta}$ are the transmission and reflection coefficients of the even-odd mode two-port networks of the hybrid excited from its sum and difference ports, the even and odd mode networks are shown in the upper and lower panels of Fig. 1(b), respectively. The ABCD matrices of the circuits in Fig. 1(b) can be calculated by multiplying the ABCD matrices of the cascading $\lambda/8$, $\lambda/4$ and $3\lambda/4$ sections. Different loss constants of $\lambda/4$ and $3\lambda/4$ sections can be introduced in the analysis. The solid lines in Figure VI. 2(a) and (b) are calculated transmission coefficient of a ring hybrid and measured transmission coefficient of a test structure similar to that in Figure VII. 5, respectively. The limited background cancellation is mainly caused by the loss difference between S_{21H} and S_{24H}.

Eq. (1) and (2) indicate that the conductor loss can be reduced by compensating the attenuation constant of the $3\lambda/4$ section through the adjustment of its metal thickness.

The dashed lines in Figure VII. 2(a) and (b) show the transmission coefficients of the structures with thickness adjustment. It is shown that significantly improved cancellation effects can be achieved at the designed frequency.

Assume an ideal compensation, $S_{21H} = -S_{24H}$, Eq. (1) becomes:

$$S_{21} = b_{out}/a_{in} = S_{21P} \times S_{21T} \times S_{21H} \times \left(S_{21MUT} - 1\right) \qquad \text{(VI.3)}$$

The MUT section can be modeled as ΔR and ΔL in series, as shown in Figure VI. 3. When $Z = \Delta R + j\omega\Delta L$ is small, S_{21} is:

$$S_{21} = -S_{21P} \times S_{21T} \times S_{21H} \times Z/2Z_0 = -S_{21P} \times S_{21T} \times S_{21H} \times \left(\Delta R + j\omega\Delta L\right)/2Z_0 \qquad \text{(VI.4)}$$

The coefficients $S_{de} = S_{21P} \times S_{21T} \times S_{21H}$ can be determined by a de-embedding structure which is identical to the upper half of the structure shown in Figure VII. 1(a) but without MUT. Then we can directly measure the resistance and inductance changes of the MUT and detect the corresponding FMR. Measurement errors of S_{de} will affect the accuracy of ΔR and ΔL, however the measurement sensitivity is not affected substantially due to the multiplication nature of Eq. (4), this is different from traditional subtraction de-embedding procedures. Figure VII. 4 shows the results of theoretical calculations and schematic simulations using Advanced Design System (ADS) for different MUT parameters. It is shown that a 0.1 Ω resistance change, which is about the signal level of a single domain wall resonance [7.12], can be detected when 60 dB or better cancellation is achieved. The theoretical and ADS results match each other well.

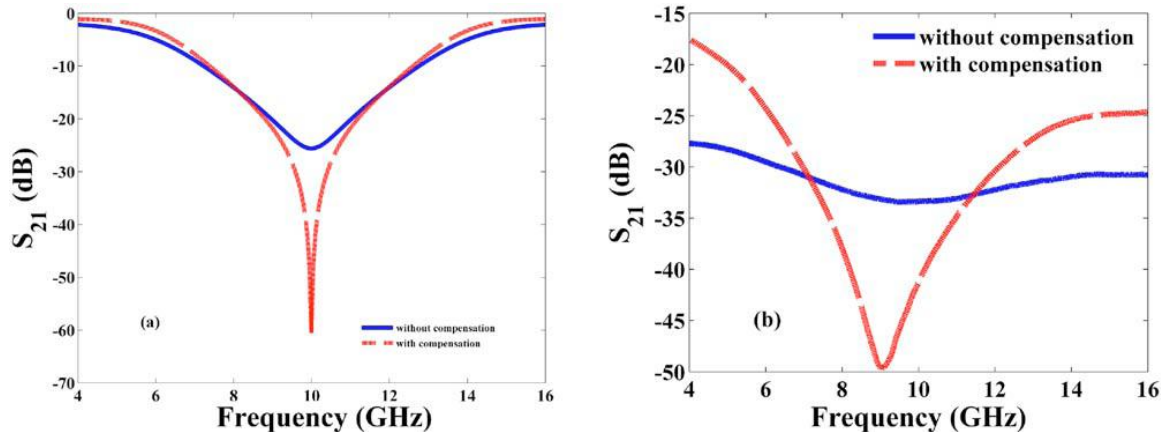

Figure VII.2 Examination of background cancellation effects. (a) Theoretical calculation results of a ring hybrid. (b) Experimental results of the structure shown in Fig. 5. Compensation is performed with a 1:3 metal thickness ratio for the λ/4 and 3λ /4 sections.

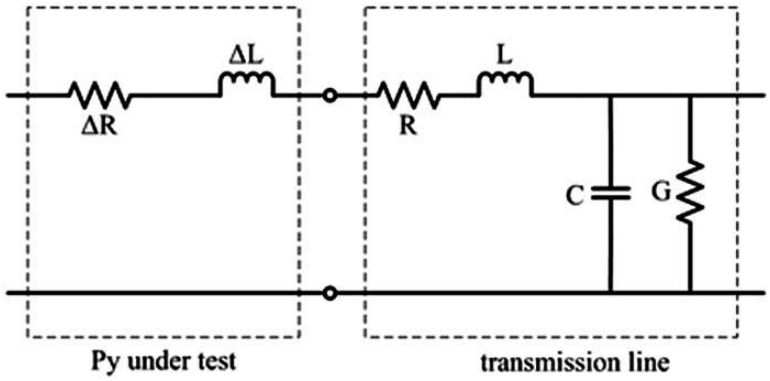

Figure VII.3 An resistance, inductance, capacitance and conductance (RLCG) model of the transmission line with ferromagnetic MUT.

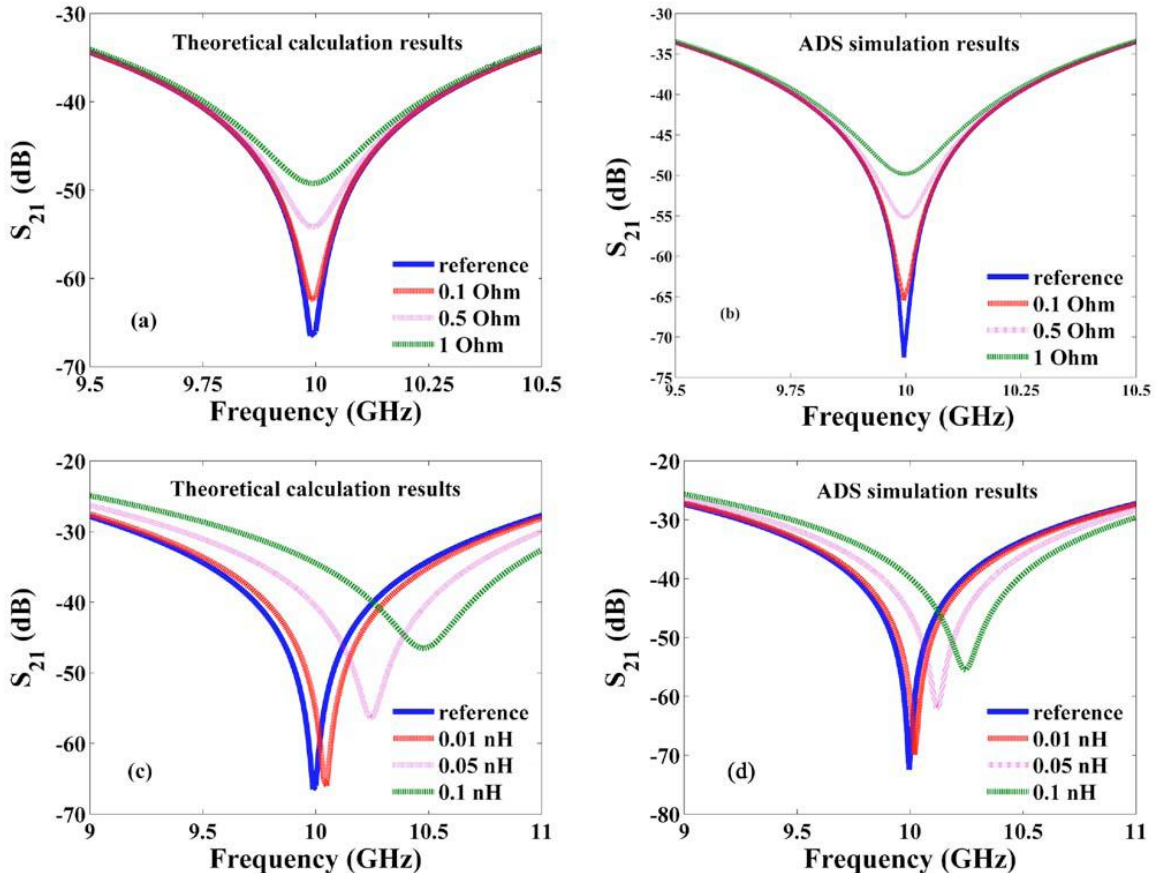

Figure VII.4 Theoretical and simulated transmission coefficients vs. different MUT parameters. [(a) and (b)] Different resistances. [(c) and (d)] Different inductances.

VII.2.2 Prototype Device Experiment Results

A prototype device of the proposed measurement structure at 10 GHz was fabricated on a 4 inch fused silica wafer, shown in Figure VI. 5. Uniplanar aluminum (Al) coplanar wave guide (CPW) was chosen to be the microwave transmission line. Coupled CPW was used to form the power divider. The signal line and gap dimensions of the transmission line section bearing the Py array are 30 μm and 4.5 μm, respectively; the thickness of the Al is 600 nm. Patterned polysilicon was used to form 50 Ω and 100

Ω resistors needed in the power divider and the hybrid. A Py array with a unit dimension of 2 μm wide, 20 μm long and 100 nm thick is placed with their easy axis along the CPW axis. The space between two adjacent Py stripes is 2 μm. All metal patterns are fabricated by standard photolithography, e-beam evaporation and lift-off processes. A microwave signal from a vector network analyzer is introduced through the input port. It generates a microwave magnetic field H_{rf} perpendicular to the Py easy axis. The output power of the network analyzer was set at -10 dBm. An on-chip short, open, load and transmission (SLOT) calibration was performed. An external DC magnetic field was slowly swept from 1200 to 300 Gauss along the Py easy axis. Due to wafer space limitations, de-embedding structures were not fabricated. But the relative S_{21} magnitudes for different bias fields are not affected as discussed above.

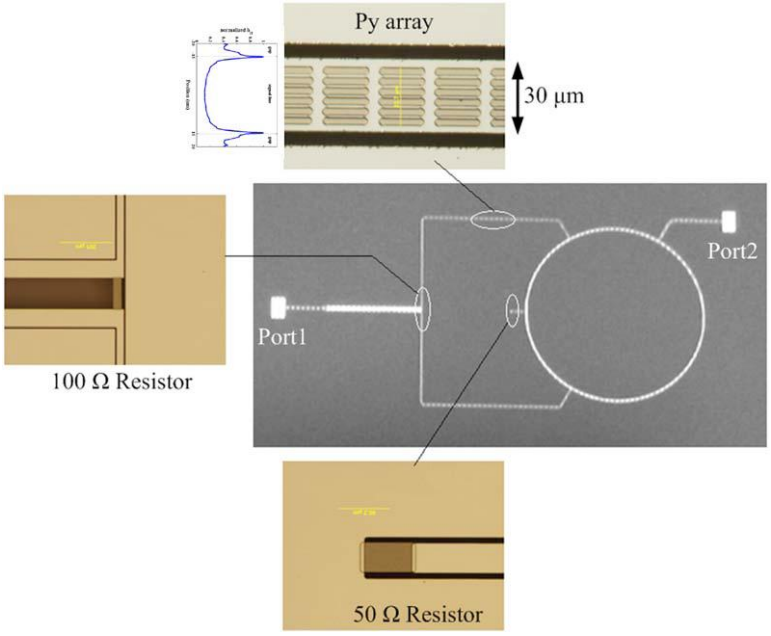

Figure VII.5 Microscope pictures of the MUT, measurement device, and its components.

The measurement results are shown in Figure VII. 6. The reference corresponds to the output under a 1500 Gauss DC magnetic field applied perpendicular to the Py easy axis. We observed that when decreasing the bias field the peak of S_{21} magnitude becomes distinctively smaller, instead of becoming bigger as shown in Figure VI. 4. This reversal of the S_{21} magnitude variation direction is due to the lack of conductor loss compensation in the $3\lambda/4$ section of the device, which results in larger loss in S_{24H}. The measured S_{21} phase shift is relatively small compared with the magnitude change which implies that the peak change is mainly caused by ΔR of the magnetic material. Eq. (4) shows that ΔR has a linear relationship with ΔS_{21}. Then we can find out the line width ΔH of the material under test by reading the full width at half maximum (FWHM) of the response, shown in Figure VII. 7(a). The frequency line width can be calculated from the following equation [7.2]

$$\Delta f = \Delta H \left. \frac{\partial f_{FMR}(H_{dc})}{\partial H_{dc}} \right|_{H_{dc}=H_d} = 1.4 \text{ GHz} \qquad \text{(VII.5)}$$

Here $\gamma = 2.8\ GHz/kG,\ 4\pi M_s = 9\ kG,\ H_d = 676\ G,\ \Delta H = 340\ G$ are used, H_d is the external magnetic field which shifts the FMR frequency of the patterned Py to the operation frequency of the device. The demagnetization factors of the fabricated Py pattern are $N_x = 0.07,\ N_y = 0.9233,\ N_z = 0.0033$, which are calculated as in [7.13]. The complex susceptibility is given by [7.14]

$$\chi(f) = -\frac{M_s\gamma^2\left(j \cdot f \cdot \alpha/\gamma + H_K + N_y M_s\right)}{\omega^2 - j \cdot f \cdot \Delta f - f_{res}^2} \qquad \text{(VII.6)}$$

The obtained Δf and $\chi(f)$ shown in Figure VII. 7(b) are comparable with the results from OOMMF [7.15] dynamic simulations of a single Py element, the damping constant of $\alpha = 0.02$ was chosen according to [7.16]. The linewidth is also in line with the previous published data [7.17]. The broad linewidth observed is due to shape anisotropy, inhomogeneous line broadening and eddy currents.

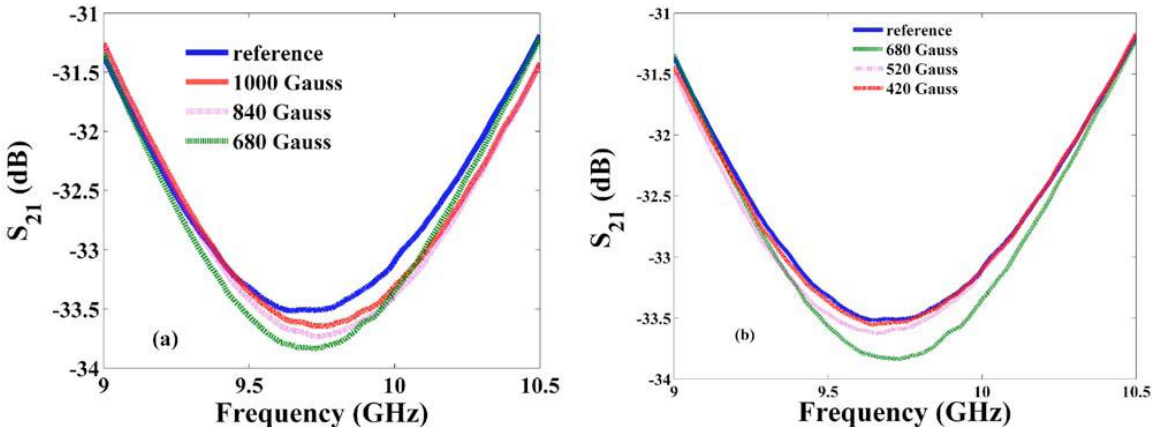

Figure VII.6 (a) *S*21 changes vs different bias fields larger than *Hd*. (b) *S*21 changes vs different bias fields less than *Hd*.

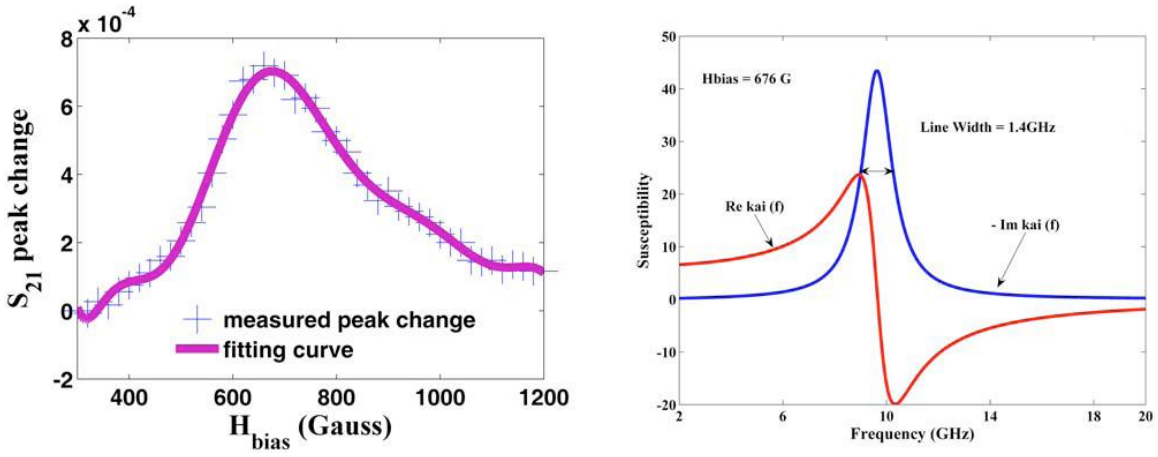

Figure VII. 7(a) *S*21 peak change at the resonance frequency of the fabricated device vs. bias field and (b) the extracted susceptibility of the tested Py array.

VII.2.3 Prototype Device Conclusions

The prototype device cancels the background parasitic signals which usually overwhelm the targeted FMR signal in a conventional FMR method. The extent of cancellation is a good indicator of signal to noise ratio improvement of the proposed method. For measurement sensitivity comparison, an individual CPW line with a Py array of 272 Py elements were fabricated and measured. The CPW line and Py elements have the same dimension as those shown in Figure VII. 5. No obvious FMR peaks were observed. One reason for the lack of the FMR observation is the relatively low CPW line sensitivity, another possible reason is the weak interaction between RF fields and Py elements since the fields are fairly weak in the middle of CPW line, the field distribution is shown in the inset of Figure VII. 5. An advanced on-chip microwave interferometer following the same principle discussed in this section is designed and fabricated. This new device will be presented in the following section.

VII.3.1 Experiment and Methods for the Advanced Device

The interferometer and the Py nanowire were fabricated by a combination of photo and e-beam lithography, e-beam evaporation and subsequent lift-off on a quartz substrate. The on-chip microwave interferometer is shown in Figure VII. 8. This structure consists of two nominally identical CPW based Wilkinson power dividers and two 100 Ω chip resistors. The resistors were attached to the interferometer with conductive epoxy for reflected power dissipation. The two paths between the two dividers (upper and bottom) have a 180 ° electrical length difference at 4.3 GHz, which is the designed working frequency f_w. A 10 μm long and 240 nm wide Py nanowire (Cr (8 nm)/Py (70 nm)/Cr (8 nm)/Au (50 nm)) is placed across the 5 μm gap on the signal line at the center of the upper path (Cr (8 nm)/ Au (50 nm)). The magnetic field generated by the microwave probing signal is concentrated at the Py nanowire. Hence, the coupling between the magnetic field and the low dimension magnetic material is enhanced [7.18]. The configuration of the center region of the bottom path is identical to that in the upper path, except that no Py layer was deposited.

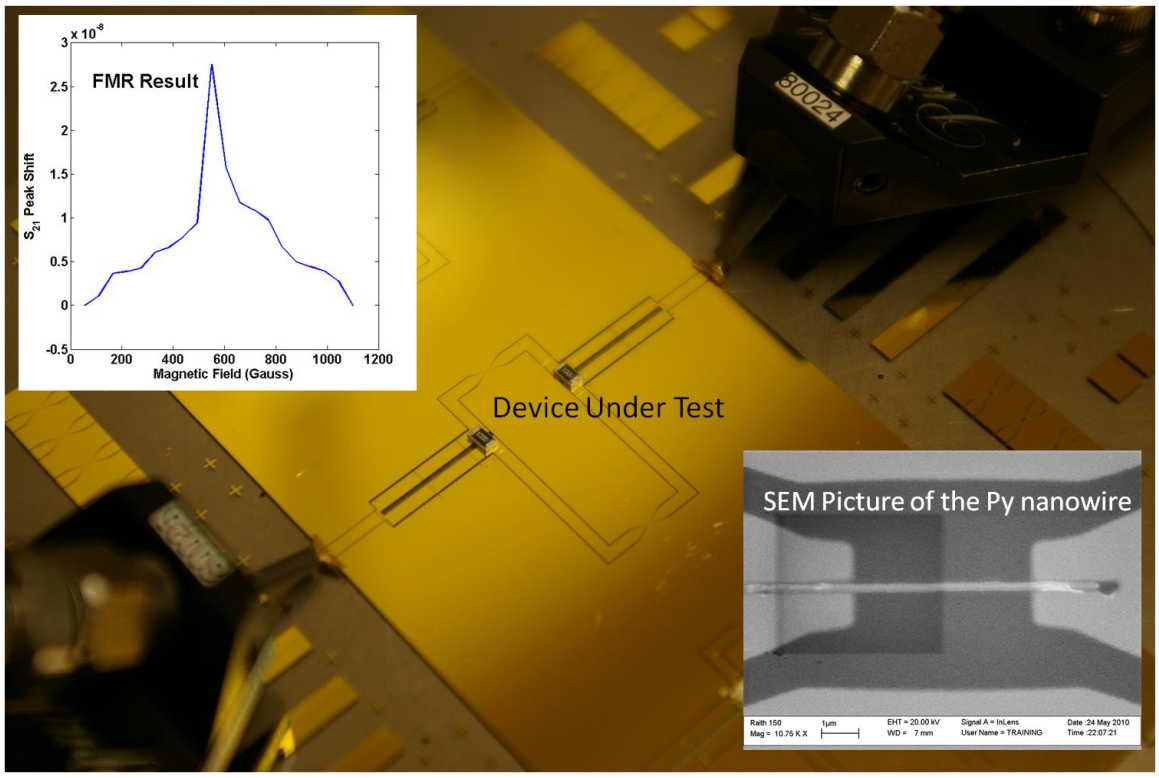

Figure VII. 8 A microscope picture for the interferometer and an SEM picture for the Py nanowire under test.

The interferometer is connected to a vector network analyzer and its transmission coefficient S_{21} is measured. The microwave signals passing through the two paths of the interferometer interfere destructively at the output port when the FMR frequency of the Py nanowire is away from f_w. A typical S_{21} is shown in Figure VII. 9. An external static magnetic field was applied perpendicular to the Py nanowire to shift its FMR frequency from the natural value $f_{FMR\_natural} = 5.5\,GHz$ to $f_w = 4.3\,GHz$. The Py FMR precession induced differences in the two signal paths will result in large changes of S_{21}. The

linewidth and damping parameters of the nanowire can be extracted from the measured relative S_{21} change.

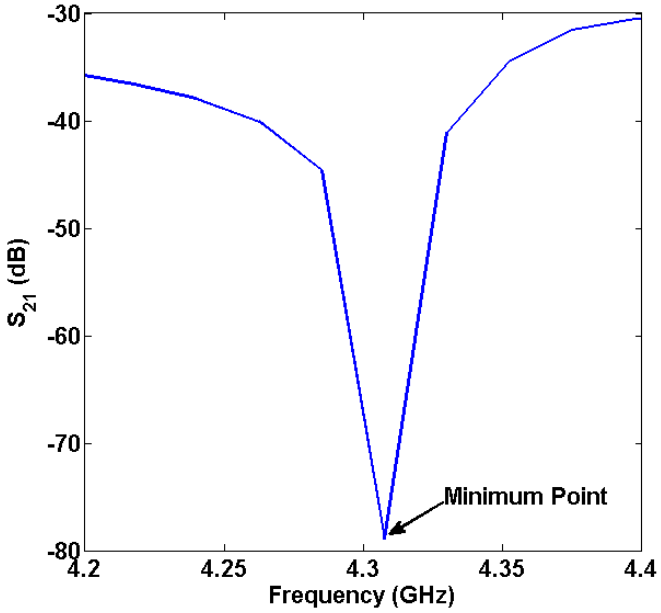

Figure VII. 9 A typical transmission coefficient S_{21} when the FMR frequency of the Py nanowire is away from the working frequency of the interferometer.

VII.3.2 Advanced Device Measurement Results and Discussions

The measured S_{21} at f_w is typically less than -77 dB as shown in Figure VII. 9 indicating an improved background noise cancellation. A 10 μm long, 240 nm wide and 70 nm thick Py nanowire was measured with the interferometer. The FMR frequency reduction process was simulated using Objective Oriented Micromagnetic Framework (OOMMF) [7.19]. The static magnetization configurations for different bias fields were first obtained. The susceptibility versus frequency plots are obtained by applying an exponentially decaying pulse field and recording the magnetization response as a

function of time. The complex susceptibility spectra are calculated by dividing the fast Fourier transform (FFT) components of the averaged magnetization in the hard axis direction with that of the applied pulse field. The results, shown in Figure VII. 10, demonstrate that when the field is around 550 Gauss the Py nanowire FMR frequency is shifted to 4.3 GHz. At this frequency the background common mode signal is strongly suppressed and the relatively large S_{21} change, due to FMR, is observed. The results are shown in Figure VII. 11. The interferometer sensitivity is defined as the relative change of S_{21} at FMR frequency to the volume of the magnetic material under test, $s = \frac{\Delta S_{21}}{\Delta V}$, compared with prototype device and a conventional transmission line methods in our previous reports [7.6] and [7.20], the sensitivity is improved by at least 20 dB with the advanced interferometer.

The linewidth ΔH can be read from the full width at half maximum (FWHM). The damping factor is extracted from equation: $\alpha = \frac{\Delta H \mu_0 \gamma}{2\omega}$, where γ is the gyromagnetic ratio and $\omega = 2\pi \times 4.3 GHz$ [7.11]. The extracted linewidth and damping constant at 4.3 GHz are 120 Gauss and 0.038, which are in line with previous results [7.22].

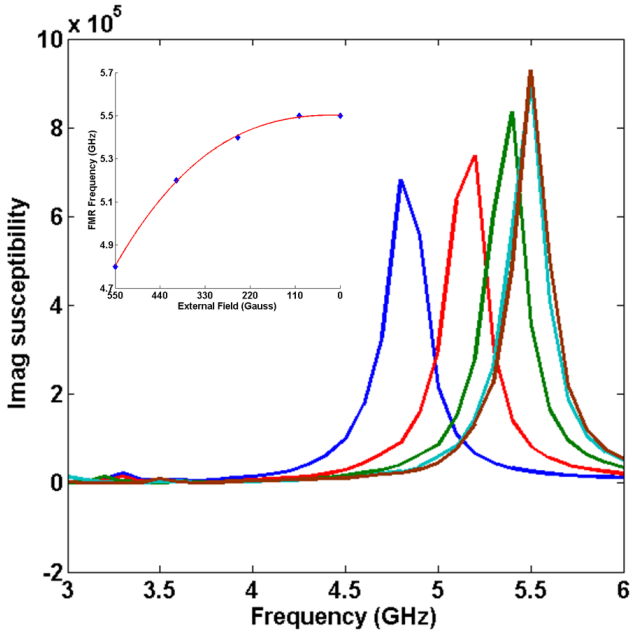

Figure VII. 10 Micromagnetic simulation results of the FMR frequency reduction process of the Py nanowire.

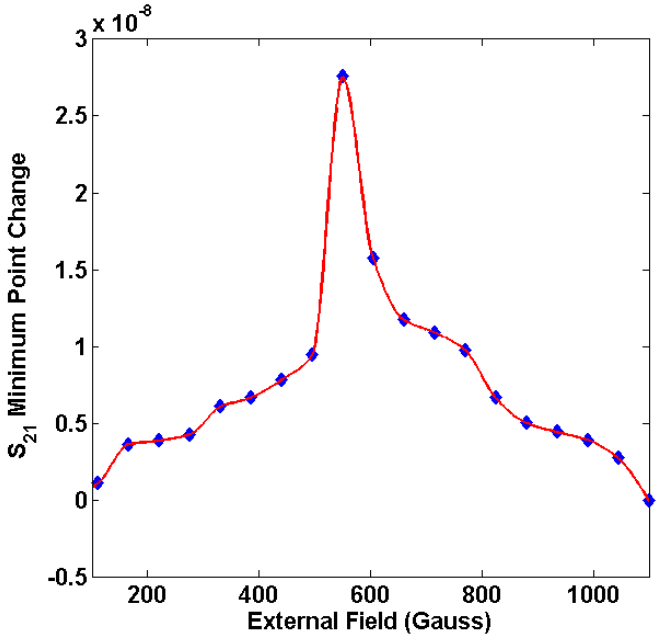

Figure VII. 11 Relative S_{21} minimum value change versus external magnetic field.

Full wave three-dimensional (3D) electromagnetic simulation (High Frequency Simulation System, HFSS) is used to model the magnetic material effects and further evaluate the interferometer performance. Assuming uniform power absorption density in the patterned Py structure, Py nanowires of different dimensions can be modeled by keeping the 3D nanowire model the same and using different magnetic loss tangent values. Hence, both fabrication and simulation difficulties that are associated with extremely small Py structures on top of a large RF structure are alleviated. The measured $0.24\times5\times0.07\,\mu\text{m}^3$ Py pattern's magnetic loss tangent can be extracted from the experimental data [7.6]. The center region of the Py nanowire test section is illustrated in Figure VII. 12. The light blue rectangle models the Py nanowire. The yellowish parts represent the gold CPW. Simulation results are shown in Figure VII. 13. When the FMR absorption is 100 times weaker, or the volume of the nanowire is 100 times smaller than the measured nanowire, the FMR response drops to the noise floor (the absolute peak value calculated at f_w) of the interferometer. Hence, nanoscale magnetic patterns and devices with a lateral size of 100 nm diameter could be characterized. This indicates that the interferometer has the potential to characterize the magnetization dynamics in lower dimensional nanomagnetic patterns, such as a typical spin-valve.

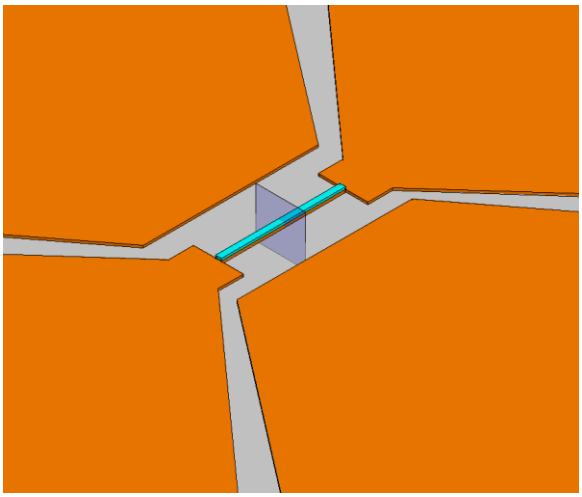

Figure VII. 12 HFSS simulation model at the center region of the Py nanowire test section, the light blue rectangle is the Py nanowire. The gray square transverse to the Py nanowire is the plane on which magnetic field distributions are recorded.

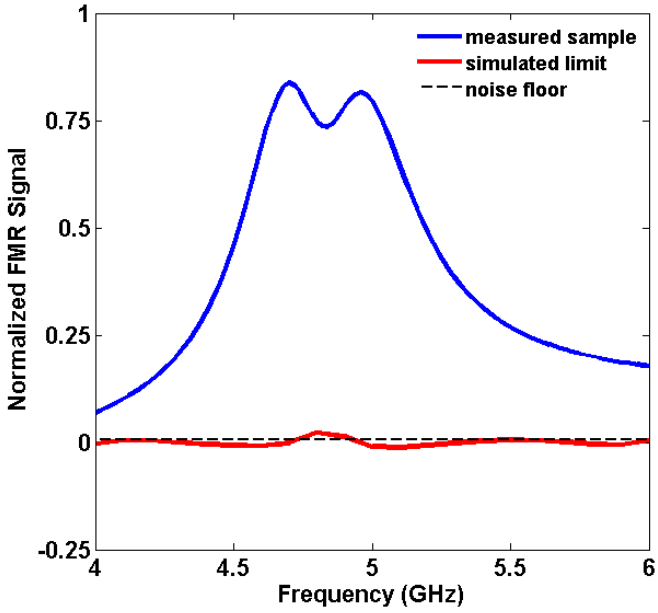

Figure VII. 13 HFSS simulation results for the FMR responses of the tested Py nanowire and a Py nanowire of 100-time weaker FMR power absorption.

VII.4 Conclusion

An ultra sensitive microwave interferometer for the characterization of magnetization dynamics of a magnetic nanowire is demonstrated. The FMR and damping properties of a single 240 nm wide Py nanowire were successfully measured. 3D HFSS simulation shows that the interferometer is sufficiently sensitive for the characterization of magnetoelectronic devices. The interferometer is also promising for fundamental nanoscale magnetic physics studies. For example, the origins of the damping in magnetic media, which were only studied in bulk materials by microwave cavity methods, can be explored with the proposed interferometer.

References

[7.1] I. Neudecker, G. Woltersdorf, B. Heinrich, T. Okuno, G. Gubbiotti, C.H. Back, "Comparison of Frequency, Field, and Time Domain Ferromagnetic Resonance Methods," *J. Magn. Magn. Mater.* **307**, 148, (2006).

[7.2] S. S. Kalarickal, P. Krivosik, M. Wu, C. E. Patton, M. L. Schneider, P. Kabos, T. J. Silva, and J. P. Nibarger, "Ferromagnetic Resonance Linewidth in Metallic Thin Films: Comparison of Measurement Methods," *J. Appl. Phys.* **99**, 093909, (2006).

[7.3] J. C. Sankey, P. M. Braganca, A. G. F. Garcia, I. N. Krivorotov, R. A. Buhrman, and D. C. Ralph, "Spin-Transfer-Driven Ferromagnetic Resonance of Individual Nanomagnets," *Phys. Rev. Lett.* **96**, 227601 (2006).

[7.4] I. Lee, Y. Obukhov, G. Xiang, A. Hauser, F Yang, P Banerjee, D. V. Pelekhov and P. C. Hammel, "Nanoscale Scanning Probe Ferromagnetic Resonance Imaging Using Localized Modes," *Nature.* **466**, 845 (2010).

[7.5] N. Mo and C. E. Patton, "Perspective: Local ferromagnetic resonance measurement techniques: "Invited Review Article: Microwave spectroscopy based on scanning thermal microscopy: Resolution in the nanometer range" [Rev. Sci. Instrum. 79, 041101 (2008)]," *Rev. Sci. Instrum.* **79**, 040901 (2008).

[7.6] H. Zhang, C. Song and P. Wang, "A New Method for High-Frequency Characterization of Patterned Ferromagnetic Thin Films," *J. Appl. Phys.* **105**, 07E716 (2009).

[7.7] C. Song and P. Wang, "A Radio Frequency Device for Measurement of Minute Dielectric Property Changes in Microfluidic Channels," *Appl. Phys. Lett.* **94**, 023901 (2008).

[7.8] Y. Yang, H. Zhang and P. Wang, "Distinguishing the Viability of A Single Yeast Cell with an Ultra-Sensitive Radio Frequency Sensor," *Lab on a Chip,* **10**, 553 (2010).

[7.9] T. Barwicz, M. R. Watts, M. A. Popović, P. T. Rakich, L. Socci, F. X. Kärtner, E. P. Ippen and H. I. Smith, "Polarization-Transparent Microphotonic Devices in the Strong Confinement Limit," *Nature Photonics.* **1**, 57 (2007).

[7.10] C. Song, Z. Liu; G. Eres, D. B. Geohegan, P. Wang, "A New Method for Microwave Characterization of Metallic Single-Walled Carbon Nanotubes," *IEEE Conference of NANO2008*, 228, (2008).

[7.11] D. M. Pozer, Microwave Engineering (Wiley, 2003).

[7.12] E. Saitoh, H. Miyajima, T. Yamaoka, G. Tatara, "Current-Induced Resonance and Mass Determination of A Single Magnetic Domain Wall," *Nature* (London) **432**, 203, (2004).

[7.13] A. Aharoni, "Demagnetizing Factors for Rectangular Ferromagnetic Prisms," *J. Appl. Phys.* **83**, 3432, (1998).

[7.14] O. Gérardin, J. Ben Youssef, H. Le Gall, N. Vukadinovic, P. M. Jacquart, and M. J. Donahue, "Micromagnetics of the Dynamic Susceptibility for Coupled Permalloy Stripes," *J. Appl. Phys.* **88**, 5899, (2000).

[7.15] M.J. Donahue and D.G. Porter, OOMMF User's Guide, Version 1.0, National Institute of Standards and Technology, Gaithersburg, MD, 1999.

[7.16] T. Korn, M. Kerekes, U. Ebels, D. Stanescu, and P. Xavier, "Pumping-Field-Induced Dynamic Effects in Micron-Sized Permalloy Lines and Their Influence on HF Filter Applications," IEEE Trans. Magn. **41**, 3514 (2005).

[7.17] B. Kuanr, R. E. Camley, and Z. Celinski, "Effect of Shape Anisotropy on Stop-Band Response of Fe and Permalloy Based Tunable Microstrip Filters," *IEEE Trans. Magn.* **40**, 2841 (2004).

[7.18] Y.-Y Au and S. Ingvarsson, "Ferromagnetic Resonance of Individual Magnetic Double Layer Microwires," *J. Appl. Phys.* **106**, 083906 (2009).

[7.19] M. Donahue and D. Porter, The Object Oriented MircoMagnetic Framework (OOMMF) Project at ITL/NIST [Online]. Available: http://math.nist.gov/oommf/2004.

[7.20] P. Wang, H. Zhang, R. Divan and A. Hoffmann, "Tailoring High-frequency Properties of Permalloy Films by Submicrometer Patterning," IEEE Trans on Magn. 45, 71 (2009).

[7.21] G. D. Fuchs, J. C. Sankey, V. S. Pribiag, L. Qian, P. M. Braganca, A. G. F. Garcia, E. M. Ryan, Zhi-Pan Li, O. Ozatay, D. C. Ralph, and R. A. Buhrman, "Spin-Torque Ferromagnetic Resonance Measurements of Damping in Nanomagnets," Appl. Phys. Lett. 95, 062507 (2007).